A Fast Surrogate Model for 3D-Earth Glacial Isostatic Adjustment using Tensorflow (v2.8.10) Artificial Neural Networks

Ryan Love[1], Glenn A. Milne[1], Parviz Ajourlou[1], Soran Parang[1], Lev Tarasov[2], and Konstantin Latychev[3]

[1]Department of Earth Sciences, University of Ottawa, Ottawa, Ontario, Canada
[2]Department of Physics and Physical Oceanography, Memorial University of Newfoundland, St. John's, Newfoundland, Canada
[3]SEAKON, Toronto, Canada

Correspondence: Ryan Love (rlove@mun.ca)

Abstract. Models of glacial isostatic adjustment (GIA) play a central role in the interpretation of various geologic and geodetic data to understand and simulate past and future changes in ice sheets and sea level, and infer rheological properties of the deep Earth. A relatively recent advance has been the development of models that include 3D Earth structure, as opposed to 1D, spherically symmetric structure. However, a major limitation in employing 3D GIA models is their high computational

5 expense. As such, we have developed a method using artificial neural networks (ANNs) and the Tensorflow library to emulate the influence of 3D Earth models with the goal of more affordably constraining the parameter space of these models: specifically the radial (1D) viscosity profile upon which the lateral variations are added.

This study provides an initial "proof of concept" assessment of using ANNs to emulate the influence of lateral Earth structure on GIA model output. Our goal is to test whether the fast surrogate model can accurately predict the difference in these outputs

10 (i.e., RSL and uplift rates) for the 3D case relative to the SS case. If so, the surrogate model can be used with a computationally efficient SS (Earth) GIA model to generate output that reproduces output from a 3D (Earth) GIA model. Evaluation of the surrogate model performance for deglacial RSL indicates that it is able to provide useful estimates of this field throughout the parameter space when trained on only $\approx 15\%$ (≈ 50) of the parameter vectors considered (330 in total). Our results indicate that the ANN:model misfits, while not negligible, are of a scale such that useful predictions of deglacial RSL changes can be

15 made.

We applied the surrogate model in a model:data comparison exercise using RSL data distributed along the North American coasts from the Canadian Arctic to the US Gulf coast. We find that the surrogate model is able to successfully reproduce the data:model misfit values such that the region of minimum misfit either overlaps the 3D GIA model results, or is within two increments in the parameter space. The surrogate model can, therefore, be used to accurately explore this aspect of the 3D

20 Earth model parameter space. While the 3D Earth models can outperform the SS Earth models for some regional subsets of the RSL data set, the SS Earth models still produce better fits overall. In summary, this work demonstrates the utility of machine learning in 3D Earth GIA modelling and so future work to expand on this analysis is warranted.

1 Introduction

Global models of glacial isostatic adjustment (GIA) have been in development since the 1970s and have several important
25 applications (e.g., Spada, 2017; Whitehouse, 2018). Broadly speaking, through comparison of model output to a variety of
both geological and geodetic data sets, they can be used to improve our understanding of ice sheet and sea-level changes on
decadal to 100 kyr timescales, and place constraints on rheological properties of the Earth's mantle. For example, geological
reconstructions of relative sea level (RSL) provide key information on past changes in regional and global ice extent during
the Quaternary (e.g., Milne, 2015). Calibrated GIA models are commonly used to predict and remove the contribution of this
30 process to observations of contemporary RSL, land motion, and gravity changes. This is done in order to better isolate signals
associated with other processes such as contemporary ice mass change (Shepherd et al., 2012) or secular changes in regional
hydrology (Steffen et al., 2008; van der Wal et al., 2008).

To date, most GIA modelling studies have applied Earth models with a spherically symmetric geometry and so capture
only variations in viscosity with depth. However, a variety of laboratory and geophysical investigations indicate strong lateral
35 variability in Earth viscosity structure at all depths in the mantle (Karato, 2008). In the past few decades, a major improvement
in the realism of GIA models has been the development of Earth models that can accommodate laterally variable viscosity
structure (e.g., Latychev et al., 2005; Paulson et al., 2005; Wu, 2005; Klemann et al., 2007; Wang et al., 2008) resulting in what
are referred to as '3D' Earth models. Since the development of these more realistic Earth models, a number of GIA studies
have shown that the influence of lateral structure is important with respect to the applications outlined above (e.g., Paulson
40 et al., 2007; Austermann et al., 2013; van der Wal et al., 2013, 2015; Kuchar et al., 2019). Therefore, it is important to continue
to apply 3D models and improve constraints on Earth viscosity structure.

A primary limitation of 3D (Earth) GIA models (hereafter simplified to "3D GIA models") is their greater computational
expense, which, in addition to the much larger parameter set associated with two additional spatial dimensions within the
Earth model, makes exploring the parameter space a major challenge. As a result, determining the optimal parameter set and
45 quantifying parameter uncertainty has not been done with any degree of rigour. The majority of studies that have applied
3D GIA models to date have focused on considering a relatively small number of 3D Earth viscosity models ($\mathbf{O}(1-10)$)
to consider the influence of the additional two dimensions on predicting surface observables (e.g., Whitehouse et al., 2006;
van der Wal et al., 2015; Powell et al., 2021). In defining 3D mantle viscosity structure, key information is provided by global
and/or regional seismic velocity models to infer lateral variability in temperature and, therefore, viscosity, and a spherically
50 symmetric (SS) model of viscosity variation on which to superimpose the lateral viscosity structure. In most studies to date,
only a handful, $\mathbf{O}(1)$, of these key model inputs have been explored. In comparison, studies focusing on the application of SS
Earth models often consider $\mathbf{O}(100)$ viscosity models and/or order $\mathbf{O}(10)$ ice loading histories to explore the model parameter
space and map out the parametric uncertainty (e.g., Steffen and Kaufmann, 2005; Love et al., 2016; Caron et al., 2017). Recent
studies using 3D Earth models have considered larger parameter sets (e.g., Bagge et al., 2021; Li et al., 2022; Pan et al., 2022),
55 however, they remain limited sample sets of the complete Earth model parameter space. One route to addressing this problem,
in terms of identifying an optimal parameter set, is using adjoint methods (Crawford et al., 2018).

The work presented here is aimed at improving our ability to explore the parameter space of 3D GIA models via the use of a machine learning tool-chain to emulate the output from a 3D GIA model. We note an important caveat for the work herein. Full emulation requires the generation of a predictive probability distribution for full model output given model inputs. To avoid name clashes between the more accurate nomenclature of surrogate model and the full 3D GIA model, we denote the surrogate model as an emulator even though it only predicts a single estimate for full model output. This approach has been employed successfully in other disciplines where model computational expense has been a limiting factor in exploring the parameter space (Tarasov et al., 2012; Sellevold and Vizcaino, 2021; Williams et al., 2023). Given the high computational expense of 3D GIA models, we seek to train a machine-learning-based emulator on a relatively small set of simulations. We view this study as developing a "proof of concept" that future studies can build upon. In this regard, we have chosen to focus this work on optimising one of the key inputs to a 3D GIA model. Specifically, for a given model of lateral structure (lithosphere and seismic model) and ice loading, we seek to determine if it is possible to successfully emulate model output for ≈ 300 different SS reference viscosity models based on a relatively small training set ($\mathbf{O}(10-100)$) simulations. Our results indicate that sufficiently precise emulation can be achieved with a training set of $\approx 40-60$ simulations, resulting in a computational (wall) time saving of $\approx 85\%$. Given this success, we considered an application of the emulator based on ~~typical a~~ GIA dataset, geological (proxy) reconstructions of RSL, to seek an optimal SS reference viscosity model for our chosen models of lateral lithosphere thickness and sub-lithosphere viscosity variations.

2 Experimental Design & Methods

Here we describe the individual components of the numerical models and overall experimental design of this investigation. We introduce, in Sect. 2.1, the individual models used, and then the method by which model output is processed to produce training data (Sect. 2.2). We then provide some details on the implementation and training of the artificial neural networks (ANNs, Sect. 2.3). Finally, we outline the data used in the proxy-data:model comparison (Sect. 2.4).

2.1 GIA/RSL Models

We use two separate GIA models to compute RSL. Both solve the sea level equation (Farrell and Clark, 1976) and model the solid Earth response to the loading and unloading of the Earth's surface through time (Mitrovica and Milne, 2003; Kendall et al., 2005). However, the RSL and solid Earth response are calculated using different numerical methods for each model. The simpler and computationally less expensive GIA model assumes a spherically symmetric (SS) structure for the Earth. Application of this model relies on the computation of visco-elastic Love numbers (Peltier, 1974) for a specified radial structure (density, elastic moduli, viscosity). Once the Love numbers have been computed (e.g., via a normal mode analysis, Peltier, 1976; Mitrovica and Peltier, 1992), calculation of various GIA observables, such as RSL, is computationally efficient. Hereafter this model will be referred to as the normal mode SS model (abbreviated to NMSS model). A model run of glacial cycle

duration typically requires less than 0.5 core-hours[1] on contemporary computer hardware (surface resolution being a key factor in determining the compute time). As a result of this computational efficiency, large scale sampling the GIA model parameter space is feasible with recent studies presenting results for many thousands of simulations exploring the parameter space of

90   Earth model and ice-sheet reconstructions (Steffen and Kaufmann, 2005; Love et al., 2016; Caron et al., 2017). The more complex and computationally expensive model that we use here - the Seakon model of Latychev et al. (2005) - does not have the limiting assumption of a spherically symmetric Earth structure. However, this model requires ≈ 1.75 core-years for a typical glacial cycle experiment, which precludes its use for generating large ensembles of model output. Contemporary investigations with the Seakon model are limited to ensembles of several dozen (e.g., Pan et al., 2022) and more typically fewer than a dozen

95   simulations.

To define a 3D viscosity structure in the Seakon model, lateral viscosity variations are applied on top of a chosen spherically symmetric (radial) viscosity model. Here we employ a commonly-used 3-layer parameterization of this spherically symmetric viscosity structure, as in the NMSS model, composed of a high-viscosity (i.e., elastic) lithosphere above two regions with uniform viscosity. These two regions are the upper mantle (base of lithosphere to ≈ 670 km depth) and lower mantle (≈ 670 km

100   to ≈ 2900 km depth). Sub-lithosphere lateral variations are applied via a set of relationships between shear-wave velocity anomalies and various depth-dependent parameters (Latychev et al., 2005, see Equations 27 through 29). Lateral lithosphere variations are typically introduced using constraints that are independent of the adopted global seismic model (see next section) and are represented as a viscoelastic layer of varying thickness with a very high (1×10^{37} Pa·s) viscosity such that the response is essentially that of an elastic layer on GIA timescales. When lateral variations are not included, Seakon model output is

105   equivalent to the NMSS model (assuming parameter values corresponding to the 3-layer viscosity structure are the same).

In order to increase the number of parameter vectors (i.e., model runs) which can be examined with the available computational resources, we use a reduced resolution configuration of the Seakon model. The reduced resolution configuration has a horizontal surface resolution of ≈ 33 km and uses ≈ 6 million nodes vs. ≈ 15 km and ≈ 17 million nodes for the default configuration. This change results in a reduction of core-time to $\approx \frac{1}{3}$ of the default configuration. As a result, we were able to explore

110   all 330 combinations of LT/UMV/LMV for which we have calculated the required Love numbers for the NMSS model, representing ≈ 150 core-years of compute resources. Comparing the differences in predicted RSL fields at various times indicates that differences are generally < 5 m at the last glacial maximum ($\approx 20,000$ years ago; Fig. S1) and diminish in amplitude for later times. Given the ~~the~~ limited spatial resolution of inputs to Seakon (e.g., ice and seismic models) and the comparatively low precision of RSL data, we consider the lower resolution grid to be sufficiently accurate for the purpose of this analysis.

115   Despite the broad overlap in function of these two models they have distinct roles in this investigation. We seek to train an ANN to simulate the difference in model output between Earth models with 3D and SS structure. This approach relies on the cheaper SS RSL solver to do much of the heavy lifting (and impose much of the physical structure) thereby strongly reducing the training data requirements for the emulator. Once the ANN is successfully trained, generating model output for a 3D Earth model is achieved by simply adding the ANN-derived 3D-SS signal to output from an efficient NMSS model with

---

[1]core-hours and core-years are equivalent to 1 hour (or year) of a CPU core at full utilization, here we generally use either Intel Xeon E5-2683 v4 Broadwell processors clocked at 2.1 GHz or AMD EPYC 7401P processors clocked at 2.0 GHz.

120 the relevant SS structure. Thus, the Seakon model is used to generate the training and validation data for the ANN component of the emulator. In comparison, the fast and computationally inexpensive NMSS model is the reference model with which the emulator output is combined to probe the parameter space beyond what is reasonable with the Seakon model.

2.2 Generation of Model Training Inputs

In order to train an ANN, an initial dataset is required from which training and validation subsets can be drawn. The Seakon
125 model is used in both SS and laterally variable/3D Earth model configurations to produce the input datasets to train the ANNs. The three primary configurations of the Seakon model used in this investigation are as follows:

- Spherically symmetric (i.e. varying only with depth and defined by 3 variables: LT, UMV, and LMV, as defined previously).

- Spherically symmetric perturbed with S-wave data from the S40RTS model [S40RTS] (Ritsema et al., 2010, plots of
130 relative viscosity variations are shown in Fig. 1)

- Spherically symmetric perturbed with S-wave data from the S40RTS model with the addition of laterally variable lithosphere thickness from the LR18 lithosphere model [S40RTS+LR18] (Ritsema et al., 2010; Afonso et al., 2019, plot of lithosphere model LR18 is shown in Fig. 1)

The fully 3D S40RTS+LR18 configuration is used for the proxy-data:model comparison and overall testing and validation
135 of the ANNs, while the semi-3D S40RTS configuration is used only for testing and comparison with the full 3D configuration. The SS configuration of Seakon is used throughout the investigation to determine the 3D-SS output on which the ANNs are trained and tested. Within each of the SS configurations we explore the parameter space of elastic lithosphere thickness (LT) as well as upper and lower mantle viscosities (UMV, LMV). The range of LT, UMV, and LMV, values used in this study are in line with previous studies which constrain these values (e.g., Lambeck et al., 2014; Roy and Peltier, 2017). The parameter space of
140 LT, UMV, and LMV values is sampled using a Latin hypercube scheme with the goal of maximizing parameter space coverage within computational resource limitations. As a result, from the combined total of 330 realizations for the S40RTS+LR18 configuration, up to 63 parameter vectors were drawn to train the ANNs while the remainder were used only for comparison against the emulator output. The configurations from which training and validation data is drawn use the same ice loading history: ICE6G (Peltier et al., 2015).

145 Separate training and validation datasets are created for each 3D configuration. Preliminary results (not shown here) indicated that emulation based on the rate of change (ROC), with respect to time, of the 3D-SS difference gives better results than emulating RSL or radial displacement (RAD) directly. Therefore, these are the datasets considered in the remainder of this analysis. These datasets were created by first differencing Seakon output for each SS configuration from the results of the associated 3D experiment (i.e., the one using the same background SS viscosity configuration). This differencing is conducted
150 using the output from the SS configuration of the Seakon model to avoid the influence of any differences between the outputs of the NMSS model and the SS configuration of the Seakon model. For each 3D-SS parameter vector we then sample the
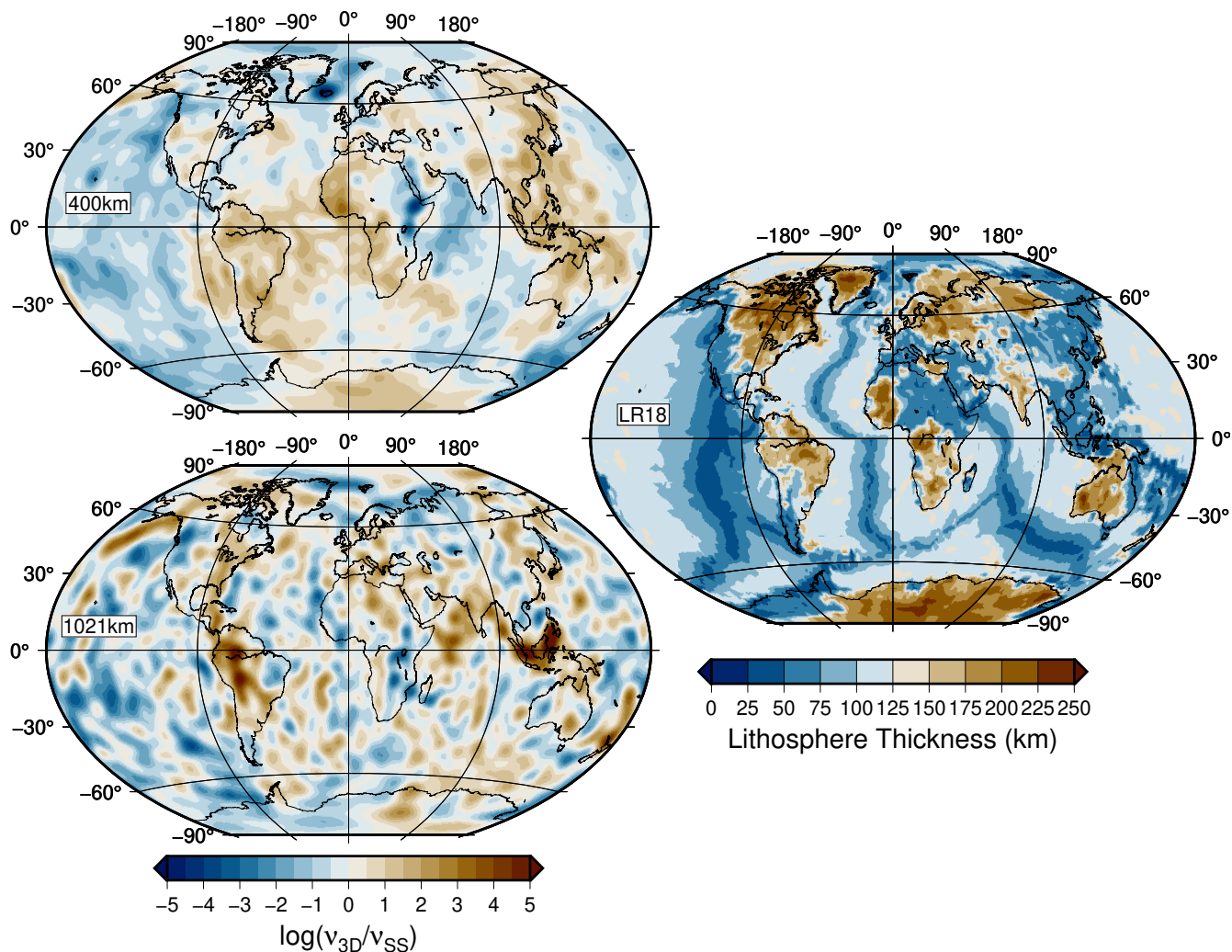
Figure 1. Left-hand panels show spatial viscosity variations as $\log(\nu_{3D}/\nu_{SS})$ for two depths in the mantle, 400 km and 1021 km. A value of zero indicates that the viscosity value at that location is equivalent to the background spherically symmetric Earth model. Right-hand panel shows the lithosphere thickness distribution of the LR18 model. Note that these thickness values are scaled such that the global average thickness is equivalent to the value specified in the SS configurations.

ROC of RSL (or RAD) at one degree regular spacing in both latitude and longitude for each model time-step (from 36 ka to present, 59 time-steps in total). For the entire ensemble (i.e., all computed parameter vectors for a given 3D configuration) we then calculate the combined probability density function of the ROC of RSL & RAD. This distribution is used to re-sample

155 the input data points of each parameter vector for more effective and efficient training of the ANNs. The distribution is used as input to a filter to selectively remove input training data-points. The filtering is implemented such that the most common values, i.e. those anomalies closest to zero largely representing far-field data, have their occurrence reduced by several orders of magnitude in the training data. This filtering reduces the input training dataset from $\approx 4,600,000$ to $\approx 500,000$ data-points per ensemble member for a given 3D configuration. The net result of this processing is a reduction of network training time,

160 computer memory requirements, and increased quality of fits in regions with larger (3D-SS) ROC RSL or ROC RAD anomalies (i.e., near- and intermediate-field locations). Each parameter vector results in a unique input training dataset file. These files are then combined as required into a single datafile for either training or validation purposes.

2.3 Training of the ANNs

The training and implementation of the ANNs is accomplished via the Tensorflow framework (v2.8.10, Abadi et al., 2015).

165 Using the datasets described in Sect. 2.2, we train separate ANNs for each of the combinations of laterally variable earth structure (i.e., S40RTS and S40RTS-LR18) and ice sheet history (i.e., ICE6G). The inputs to the ANNs can be grouped into 4 aspects: radial viscosity model, location, ice loading, and SS input data. More specifically, the ANNs are provided the thickness of the elastic lithosphere, upper and lower mantle viscosities, longitude and latitude of the data point, ice thickness and age for the location at the current and previous 4 time-steps, and finally the ROC of RSL or RAD prediction from the SS configuration

170 of the Seakon model. The output of the ANNs is the 3D-SS anomaly for the ROC of either RSL or RAD at the location and time which corresponds with the input to the ANN. ANN training and model construction (i.e., specification of size and number of hidden layers) is done via the Keras Application Programming Interface. Training of an individual ANN usually requires no more than a dozen hours of wall time using a single NVIDIA P100 Pascal Graphics Processing Unit (GPU). The training of a given ANN is iterated until an early stopping condition, based upon the the mean square error of the model against the training

175 dataset, is activated. This approach is used to prevent, or at least minimize, over-fitting of the trained ANNs (Chollet, 2021). We note there was no evidence of over-fitting in the training diagnostics.

With the Keras Application Programming Interface we construct multi-layer perceptron feed-forward ANNs. The structure of the ANN is composed of an input layer, 8 fully connected hidden layers of width 512, followed by 8 fully connected hidden layers of width 256, followed by the output layer. Between the fully connected hidden layers are normalization layers which

180 shift and scale their inputs such that the resulting distribution has a mean of 0 and a standard deviation of 1. The addition of the normalization layers helped with convergence of the network as network depth increased. A variety of ANN structures (layer counts from 1 to 20 layers and widths from 8-1024, in steps of 2^n, were varied using an initial test dataset) were evaluated and this configuration resulted in a good balance between performance and training expense. The python scripts used for training and implementing the ANNs for producing various GIA predictions are available as supplemental materials.

2.4 Model:Data Comparison - Source Data and Analysis Methods

For the RSL proxy-data:model comparison we use the RSL databases of Engelhart and Horton (2012), Love et al. (2016), and Vacchi et al. (2018), which spans the eastern North American coastline from the Canadian Arctic to the US Gulf Coast. Combined, these databases contain > 2500 sea level index and limiting points for the early to late Holocene. The locations of these data points are shown in Fig. S2.

In order to quantify the RSL misfits we use the same metric as in Baril et al. (2023) for sea level index points (SLIPs) and limiting data, reproduced here for reference.

$$\delta_{SLIP} = \frac{1}{N}\sqrt{\sum_{n=1}^{N}\left(\frac{RSL_{data,n}-RSL_{model,n}}{\Delta_{RSL,n}}\right)^2 + \left(\frac{t_{data,n}-t_{model,n}}{\Delta_{t,n}}\right)^2} \tag{1}$$

$$\delta_{limit} = \frac{1}{N}\sqrt{\sum_{n=1}^{N}\left(\frac{RSL_{data,n}-RSL_{model,n}}{\Delta_{RSL,n}}\right)^2} \tag{2}$$

In equation 1, the $RSL_{model,n}$ and $t_{model,n}$ values are the model RSL and time-value from the point of closest approach of the model curve to the value of the SLIP. However, for limiting data, the misfit (equation 2) is calculated using the same time value as the data point itself. In the case of limiting data, if the RSL curve for a given model falls above/below a marine/terrestrial data point within the range of dating uncertainty, then the misfit for that data point is set to zero (Baril et al., 2023). When examining the total δ for a given RSL database, the following values are provided: δ_{SLIP}, δ_{ML}, δ_{TL}, and δ_{Total}. Where δ_{SLIP} is the value from equation 1 for a given SLIP database, δ_{ML} and δ_{TL} are the values from equation 2 for marine and terrestrial limiting data respectively, and $\delta_{Total} = \delta_{SLIP} + (\delta_{ML} + \delta_{TL})/2$. Contributions from limiting data are normalised by two since these data only provide one-sided constraints on RSL.

3 Results and Discussion

3.1 Network training and performance

In this section we determine how many parameter vectors are required to obtain usefully accurate predictions from the emulator (we use 'emulator' here to refer to the combination of trained ANNs with output from the NMSS model). In order to estimate this number we construct several ensembles consisting of increasing quantities of parameter vectors in the training dataset. These ensembles were constructed using the Seakon configuration utilizing the S40RTS model to construct lateral viscosity variations in the mantle with lithosphere variations derived from the LR18 model. Each trained ANN incorporated the same set of 9 extreme ensemble members (i.e., members that include LT/UMV/LMV parameter values at the end of the ranges explored in the initial sampling). Additional members were added to this baseline set resulting in 4 trained networks with N = 18, 27, 45, and 63 members, respectively. To quantify the generalization of the ANNs (i.e. their accuracy with respect to parameter vectors not in the training ensemble) as a function of training ensemble size, the mean square error (MSE) for each parameter

vector in the LT/UMV/LMV space is calculated. The MSE for a given parameter vector is averaged over all locations and
215 time-steps (i.e. the full dataset described in Sect. 2.2).

Plots of the MSE through the LT/UMV/LMV parameter space for the ROC RSL are shown in Fig. 2 for the different training
sub-ensembles (although, results for $N = 18$ are not shown). It is notable that the reduction in the MSE in going from $N = 27$
to $N = 45$ is more marked compared to the change from $N = 45$ to $N = 63$. This indicates that $N = 45$ is close to an optimal
value in terms of performance (lowering the MSE) versus the size of training set. In general, throughout the parameter space,
220 the MSE decreases as the number of members in the training set increases (this is particularly evident when considering the
median and lowest MSE values) Furthermore, these plots show that the thickness of the elastic lithosphere is generally a weak
predictor of the 3D-SS ROC RSL. In general, regions in the parameter space that have at least one member from the training
ensemble, independent of the LT value, have lower MSE values compared to those with none. This finding is also supported
by the input layer weights, where LT is consistently the lowest weight input (and thus has the lowest impact on predictions)
225 across multiple ANNs. Figure 2 also shows that prediction accuracy for a given parameter vector is generally larger when it is
adjacent to another which is part of the training ensemble. These features indicate that the ANN has useful levels of predicative
ability when considering LT/UMV/LMV values outside the training dataset.

Despite the MSE of the full spatio-temporal datasets being a useful metric for comparing between different ANN archi-
tectures and training ensembles, it is of limited utility in describing the effectiveness of a given ANN in reproducing the
230 geophysical output of interest. Therefore, plots showing the difference between emulated output versus modelled output (for
S40RTS+LR18) are provided for the RSL field at 10 ka (Figs. 3 and S3) and the uplift rate at present day (Figs. 4 and S4).
They show RSL and ROC RAD predictions for the parameter vector which has the median MSE from the validation (i.e., not
used as part of the ANN training) sub-ensemble for the $N = 45$ case. In addition, plots of the predicted RSL time series are
shown for the emulated and model-predicted output (and the difference) in Fig. 5.

235 Comparing the scale of emulator:model anomaly to the RSL field itself (Fig. 3) we see that the misfit is $\mathbf{O}(1\,\mathrm{m})$ where
generally the RSL field itself is generally $\mathbf{O}(10 - 100\,\mathrm{m})$. The intermediate-field region (e.g., proximal and south of the zero-
contour in Fig 3) is problematic, as the emulator:model anomaly does not decrease with the same spatial pattern as the RSL
field itself (although it does broadly share the same spatial pattern), thus there is a region where the anomaly is comparable to
the RSL field itself. The spatial distribution of the emulator:model anomaly for RSL does not have a clear source, such as the
240 shear-wave velocity anomaly from S40RTS or lithosphere thickness (as shown in Fig. 1); although it is important to note that
the sub-lithosphere (lateral) viscosity variations change with depth and so the patterns shown are only representative within
limited depth ranges. The magnitude of the pattern scales with that of RSL, and so the ice-loading history is one controlling
factor.

Examining the timeseries data in Fig. 5 we obtain similar findings to those of Fig. 2 in that the emulator:model misfit de-
245 creases as the number of parameter vectors in the training dataset increases. This finding is consistent across ice covered/near-
field, intermediate-field, and far-field regions. The intermediate-field (e.g., Northern South-Carolina) is the most difficult por-
tion of the field to emulate. The results show that ≈ 45 training members are generally sufficient to reproduce RSL using 3D
Earth models for the ice covered/near field, intermediate, and far field regions shown here. Examination of results using fewer
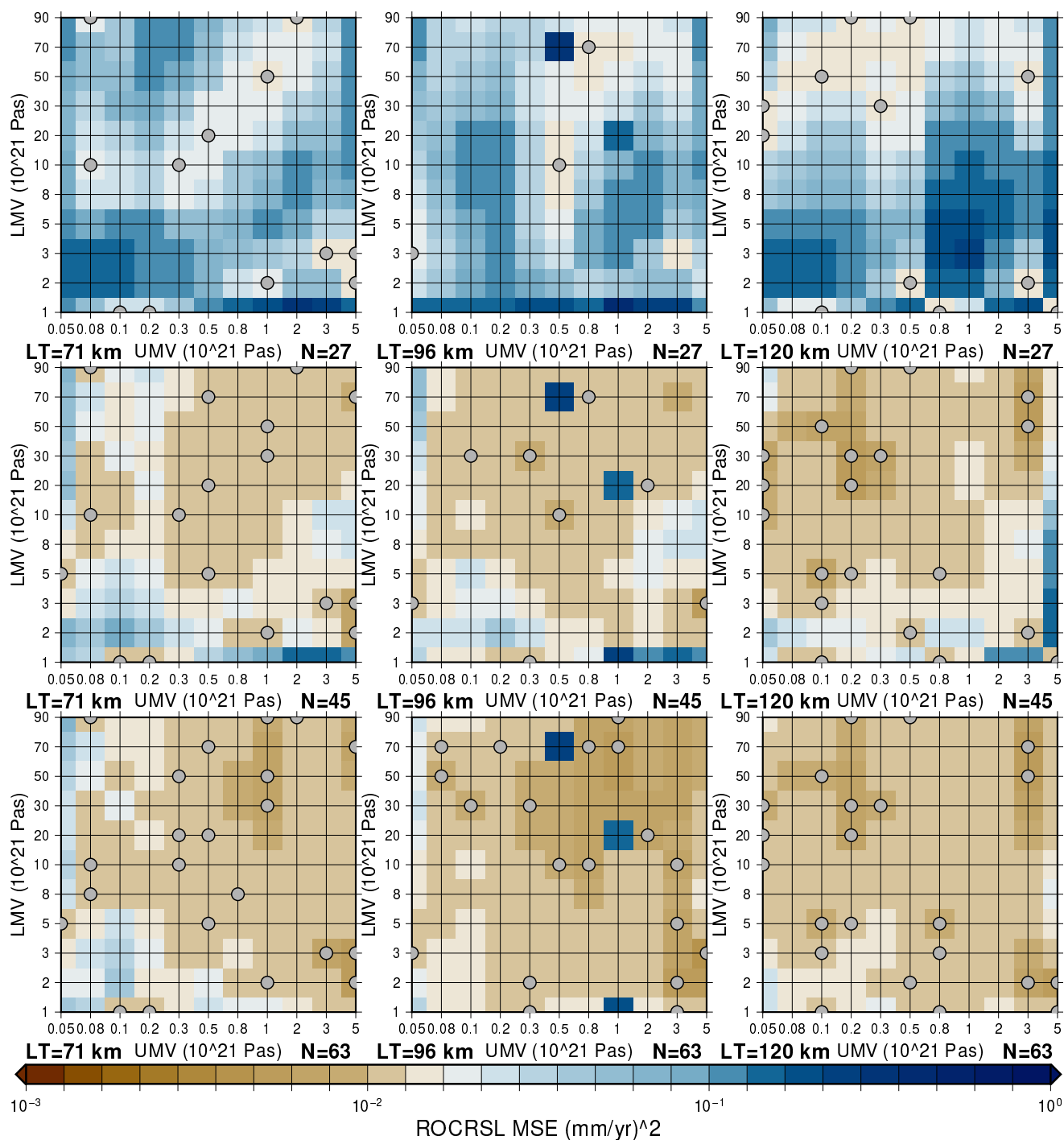
Figure 2. Plot shows the MSE (for all locations and time-steps) through parameter space (LT/UMV/LMV) for input training datasets with N=27 (top row), 45 (middle row), and 63 (bottom row) for the S40RTS+LR18 ROC RSL ANN. Parameter vectors included in training dataset are indicated by grey circles. Columns give results for the three values of global-mean elastic lithosphere thickness: 71 km (left), 96 km (middle), 120 km (right).

training members (N = 18, not shown) also indicates that fewer training members may be required for regions with greater

250 density of training data (e.g., ice-covered regions). For the N = 18 case, misfits for Hudson's Bay are of the same **O**(m) misfit
for this smallest training ensemble size. We note that, site depending, the difference in predicted RSL between the emulator
and the Seakon results is generally small (i.e., of the same scale as proxy-data uncertainties) during the Holocene, the time
interval for which the majority of RSL data exist.

When examining the emulator:model anomaly for contemporary uplift rates we find this method to be less accurate in

255 comparison to RSL. The anomalies are generally of the same order of magnitude as the total modelled uplift rates for most
regions (see Figs. 4 and S4). However, the overall MSE results (e.g., as shown for ROC RSL in Fig. 2) are comparable when
examined over the whole spatio-temporal dataset and so performance comparable to that for RSL is obtained for earlier time
intervals (Fig. S5). The spatial distribution of the emulator:model anomaly for present day ROC of RAD more closely follows
the overall distribution of the 3D Earth model's uplift field compared to the RSL results. While not investigated here, we

260 propose the poorer results for this model output are a result of the construction of the ANNs and training dataset. Firstly, the
ice sheet history represents over half of the input vector to the ANN and predictions of the 3D-SS uplift difference have no
change in ice sheet history within the time range used to emulate ROC of RAD at present day (previous 4 time steps; for
ICE-6G these are 0.5, 1.0, 1.5, and 2.0 ka). The training dataset is mostly composed of data with larger amplitude signals.
Restricting the training data input to the ANNs, or providing alternate ice history information (e.g., maximum ice thickness

265 at that location within the last 10 ka) may provide greater ANN accuracy. Given the relatively low accuracy of our results for
contemporary uplift rates we do not conduct data:model comparisons in Sect. 3.2.

Comparing the above results to those for the simpler 3D Earth model case, i.e., S40RTS with a SS lithosphere, we find
similar amplitudes of emulator:model misfit with respect to contemporary uplift rates. The emulator:model misfit for RSL is
generally smaller for the same number of training parameter vectors for this simpler Earth model - of particular note is that

270 performance within intermediate-field locations is improved (see Fig. S6). Without exploring additional 3D Earth models we
cannot conclude if this feature is a result of considering a simpler Earth model which does not incorporate the spatially variable
elastic lithosphere, or our methodology (e.g., network training or architecture). Despite this, of the configurations tested here,
we find similar numbers of parameter vectors are required in the training dataset to obtain usable accuracy even for this simpler
3D Earth model.

275 Overall, we are able to successfully reproduce the influence of 3D Earth structure using ANNs trained using 45, or more,
parameter vectors (out of a total of 330 for the LT/UMV/LMV values considered here) when considering past RSL and uplift
rates. However, model:emulator misfits are generally of the same order of magnitude of the uplift rate field when considering
contemporary uplift rates. As such, the emulator developed here is of limited utility for comparisons to contemporary uplift
rates derived from GNSS data.

280 Two logical extensions to this methodology became apparent over the course of this investigation. The first extension would
be to implement a probabilistic Bayesian artificial neural network (BANNs, e.g. as described in Jospin et al., 2022). A BANN
can provide estimates regarding the accuracy of a given prediction. Given that any error in the ROC of RSL or RAD propagates
throughout the whole prediction (with respect to time), this information could be used to potentially reduce emulator:model
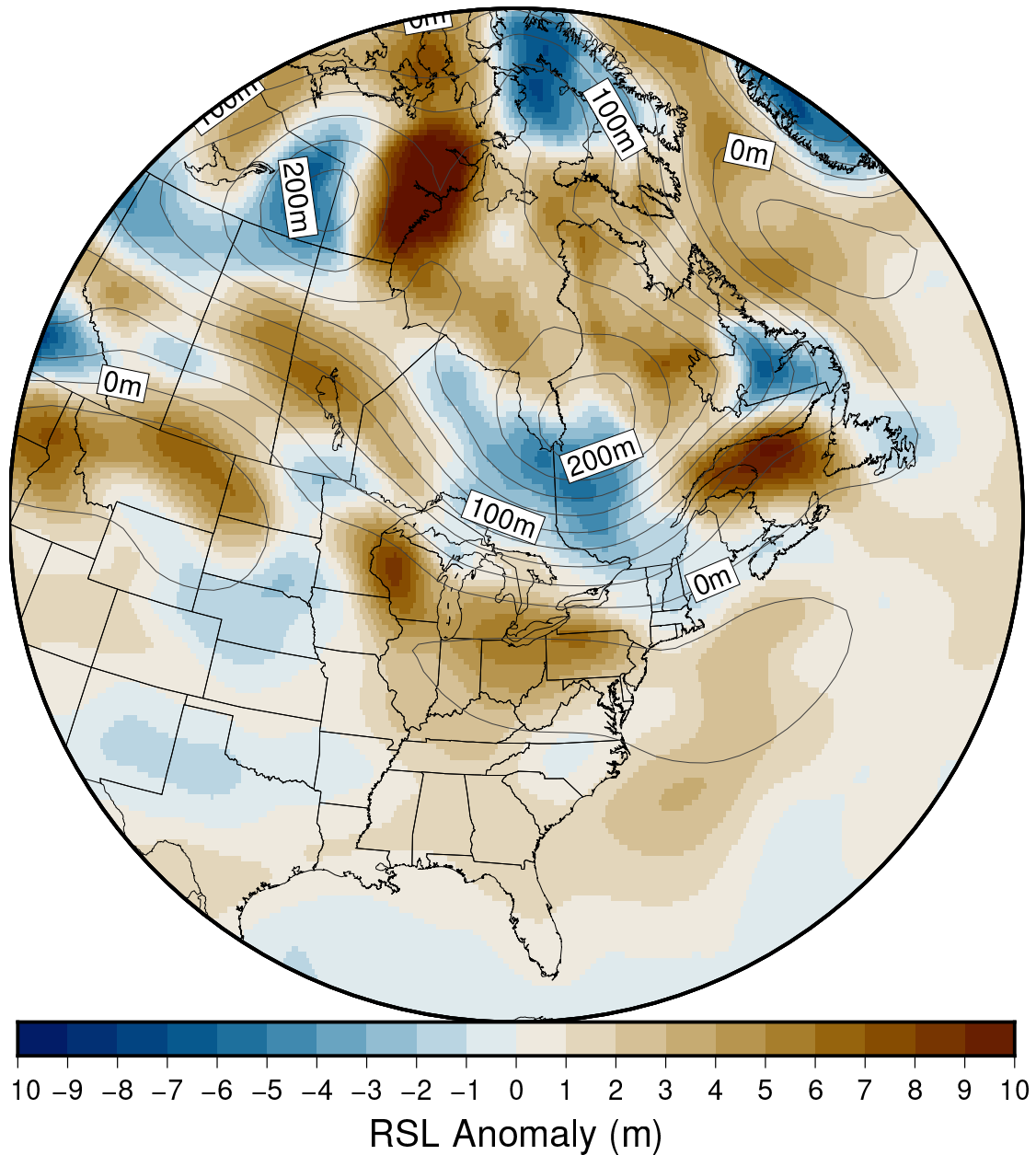
Figure 3. RSL anomaly: emulated RSL field minus explicit (3D-SS Seakon + NMSS) RSL field for the S40RTS+LR18 case, at 10 ka. Contours denote the RSL field (from the explicit case) in 25 m increments. The parameter vector plotted is that with the median MSE, calculated for all spatio-temporal data, for the N = 45 ANN. A global map of the same field is shown in Fig. S3
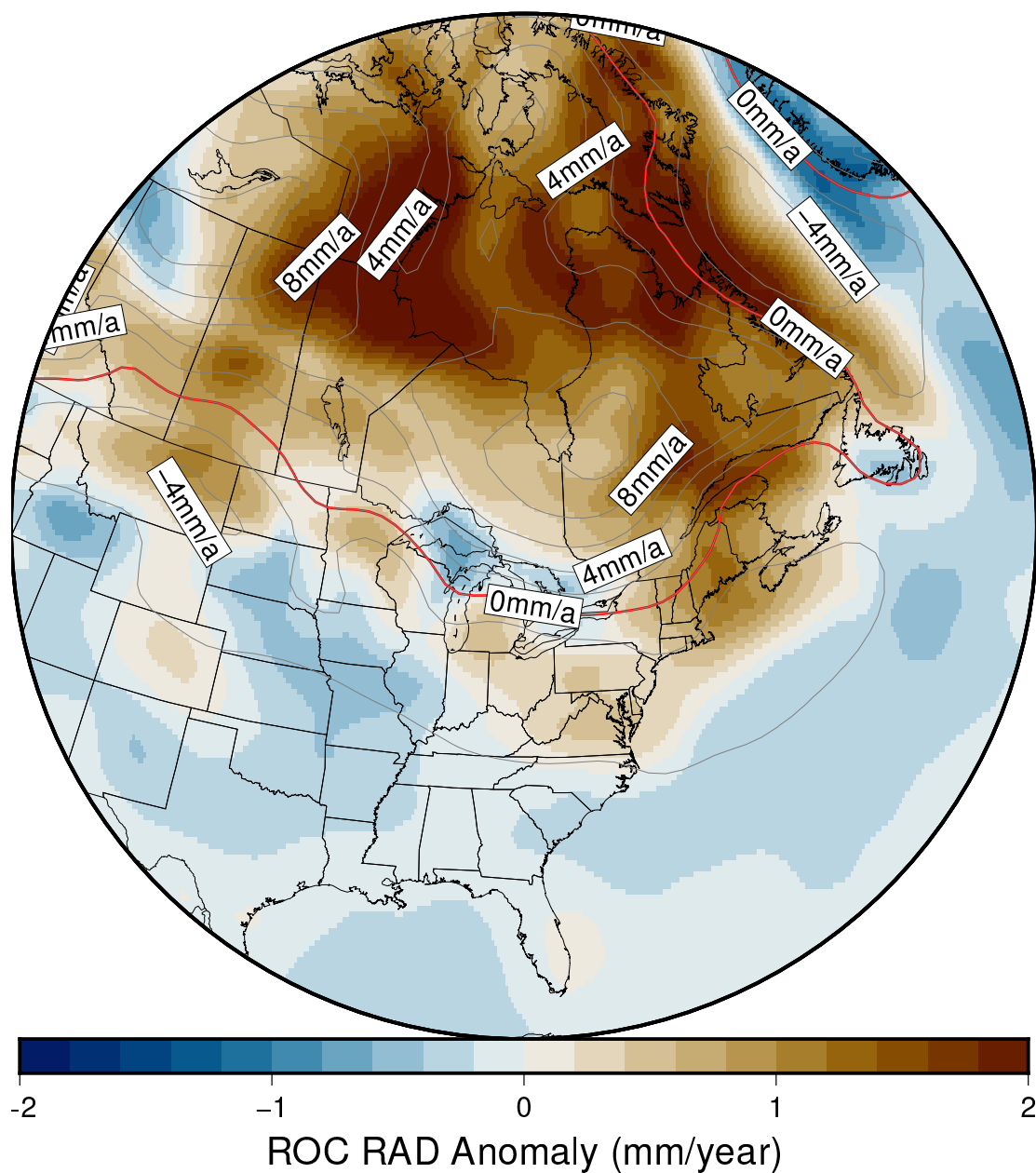
Figure 4. ROC RAD anomaly, emulated RSL field minus explicit (3D-SS Seakon + NMSS) field for the S40RTS+LR18 case at present day. Contours denote the total, modelled ROC RAD field (from the explicit case) in 2 mm/yr increments, the red line denotes the 0 mm/yr contour. The parameter vector plotted is that with the median MSE, calculated for all spatio-temporal data, for the N = 45 ANN. A global map of the same field is shown in Fig. S4, and an equivalent map but for 10 ka is shown in Fig. S5.
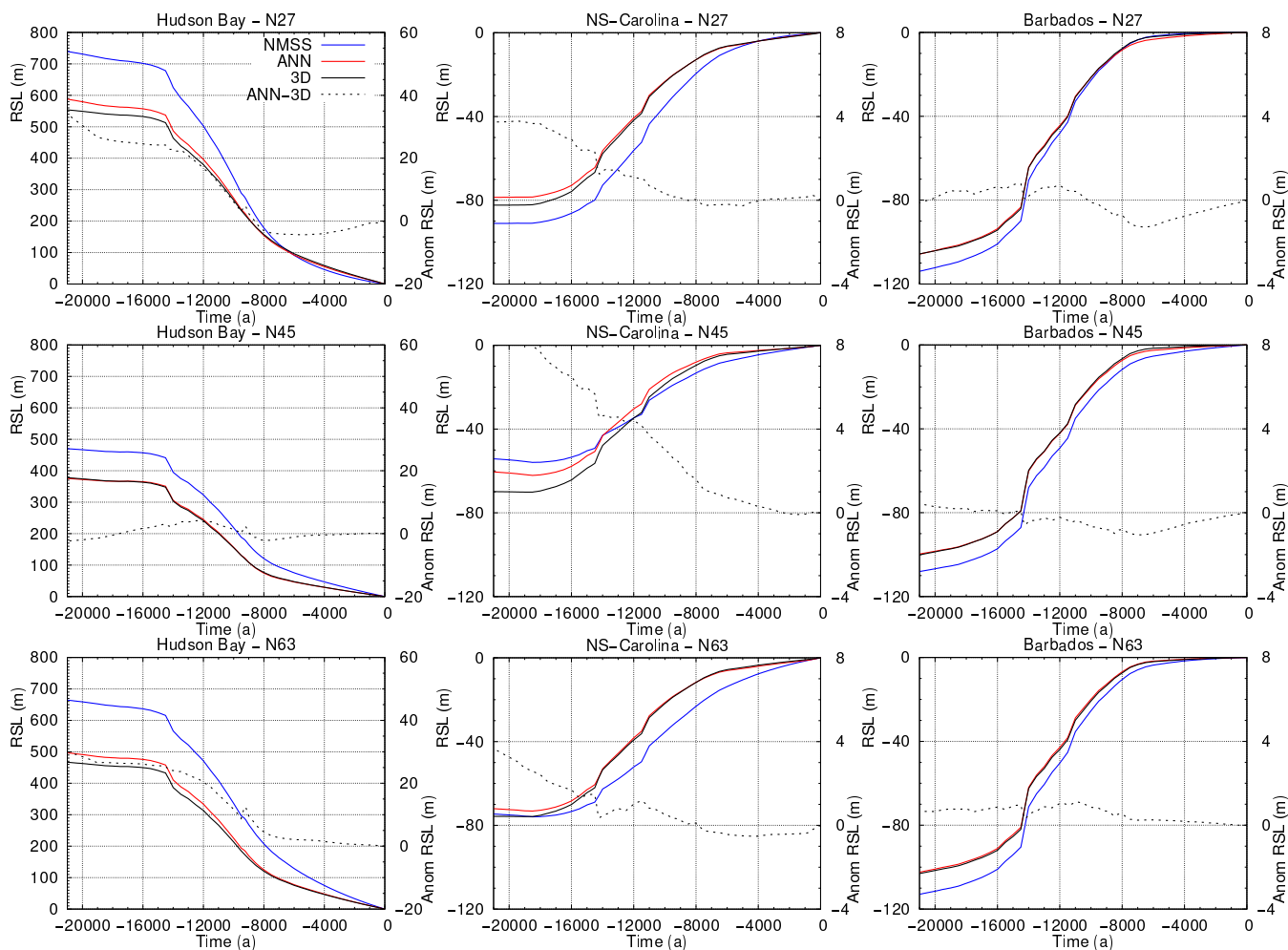
Figure 5. RSL timeseries for a near- (Hudson Bay), intermediate- (Northern S-Carolina), and far-field (Barbados) locations, for the N=27, 45 and 63 ANN training sets. Parameter vectors shown are drawn from the validation ensemble and are the median members (when considering the full spatio-temporal mean square error of the ANN). The 3D Earth model configuration shown is S40RTS+LR18. Note that since the parameter vectors correspond to the median member of the validation ensemble, the RSL curves themselves vary between N values.

misfits (e.g., via a cut-off where the ANN is not employed for a given prediction if the prediction confidence were too low).
285 The second extension would be to train the ANNs on multiple ice sheet histories in order to generalize their predictions across variations of this input parameter. Doing so requires no changes to the ANN or training data construction, simply conducting and processing additional Seakon simulations with multiple ice sheet histories. A brief exploration, not shown here, using the ANNs trained on the ICE6G ice sheet history to emulate model output corresponding with the ANU ice sheet reconstruction (Lambeck et al., 2014) resulted in large emulator:model RSL differences. This aspect of the emulation is a target for future
290 work.

3.2 Use of Emulator to Identify Optimal SS Viscosity Model

The emulator (i.e., the ANNs in combination with the NMSS model) is used here to examine the effects of imposing 3D viscosity variations, specifically those from the S40RTS+LR18 configuration, on reconstructions of RSL and associated inferences of Earth structure. The ANNs used with the emulator were trained using 45 parameter vectors, as identified in Sect. 3.1, to provide
295 a balance between computational expense and accuracy. As part of the validation process for the emulator and to assess the scale of impacts resulting from emulator:model differences, we calculate the proxy-data misfit values (as in Sect. 2.4) for the combined NA RSL database for three different sources of model output: the NMSS model, the NMSS model combined with emulated 3D-SS output, and the NMSS model combined with explicit 3D-SS Seakon output. The results of these calculations, considering the total misfit (i.e., all RSL proxy data types), are shown in Fig. 6. Misfit values for SLIPS, limiting data, and all
300 data are shown in Fig. S7 for the explicit (3D-SS+NMSS) output, with comparable misfit plots for the emulator output in Fig. S8 and the NMSS model output in Fig. S9. Comparing the bottom two rows of Fig. 6 we find that the emulator largely captures the impact of 3D viscosity structure (using the results for the NMSS model (top row) as a reference), but does not result misfit values that are indistinguishable with those determined from the explicit output. The emulated results are, upon visual inspection, more similar to the explicit results than the NMSS results alone. To evaluate the effectiveness of the emulator across the
305 entirety of the LT/UMV/LMV parameter space we use the MSE of the proxy-data:model misfit between the emulator and the explicit data, and the emulator and the NMSS data. That is, for the emulator:NMSS MSE,

$$\text{MSE}_{\text{emulator:NMSS}} = \frac{1}{n_{\text{LT}}n_{\text{UMV}}n_{\text{LMV}}} \sum_{\text{LT}=1}^{n_{\text{LT}}} \sum_{\text{UMV}=1}^{n_{\text{UMV}}} \sum_{\text{LMV}=1}^{n_{\text{LMV}}} \left(\delta_{\text{total}}^{\text{emulator}}(\text{LT},\text{UMV},\text{LMV}) - \delta_{\text{total}}^{\text{NMSS}}(\text{LT},\text{UMV},\text{LMV}) \right)^2 \quad (3)$$

where $n_{\text{LT}}, n_{\text{UMV}}, n_{\text{LMV}}$ are, respectively, the number of LT, UMV, and LMV values in the explored parameter space, and $\delta_{\text{total}}^{\text{emulator}}, \delta_{\text{total}}^{\text{NMSS}}$ are the total misfit values as described in Sect. 2.4 for the emulator and NMSS data respectively. The MSE
310 provides a metric which allows for comparison of the calculated proxy-data:model misfits for the emulator, NMSS, and the explicit results. In the ideal case of the misfits calculated using the emulator being identical to those from the explicit data the emulator:explicit MSE would be zero. MSE values for the SLIP data demonstrate that the the emulator misfits are closer to those of the explicit model ($\text{MSE}_{\text{slip}} = 0.74 \times 10^{-3}$) than the NMSS model ($\text{MSE}_{\text{slip}} = 7.11 \times 10^{-3}$) as indicated in Fig. 6.

Upon subdividing the coastline into the three regional databases (as in the studies which present the datasets): the Canadian
315 Arctic-Atlantic Coast (CAAC, Vacchi et al., 2018), the US-East Coast (USEC, Engelhart and Horton, 2012), and the US Gulf Coast (USGC, Hijma et al., 2015; Love et al., 2016), we find similar results (Figs. S10, S11, and S12) to those the total
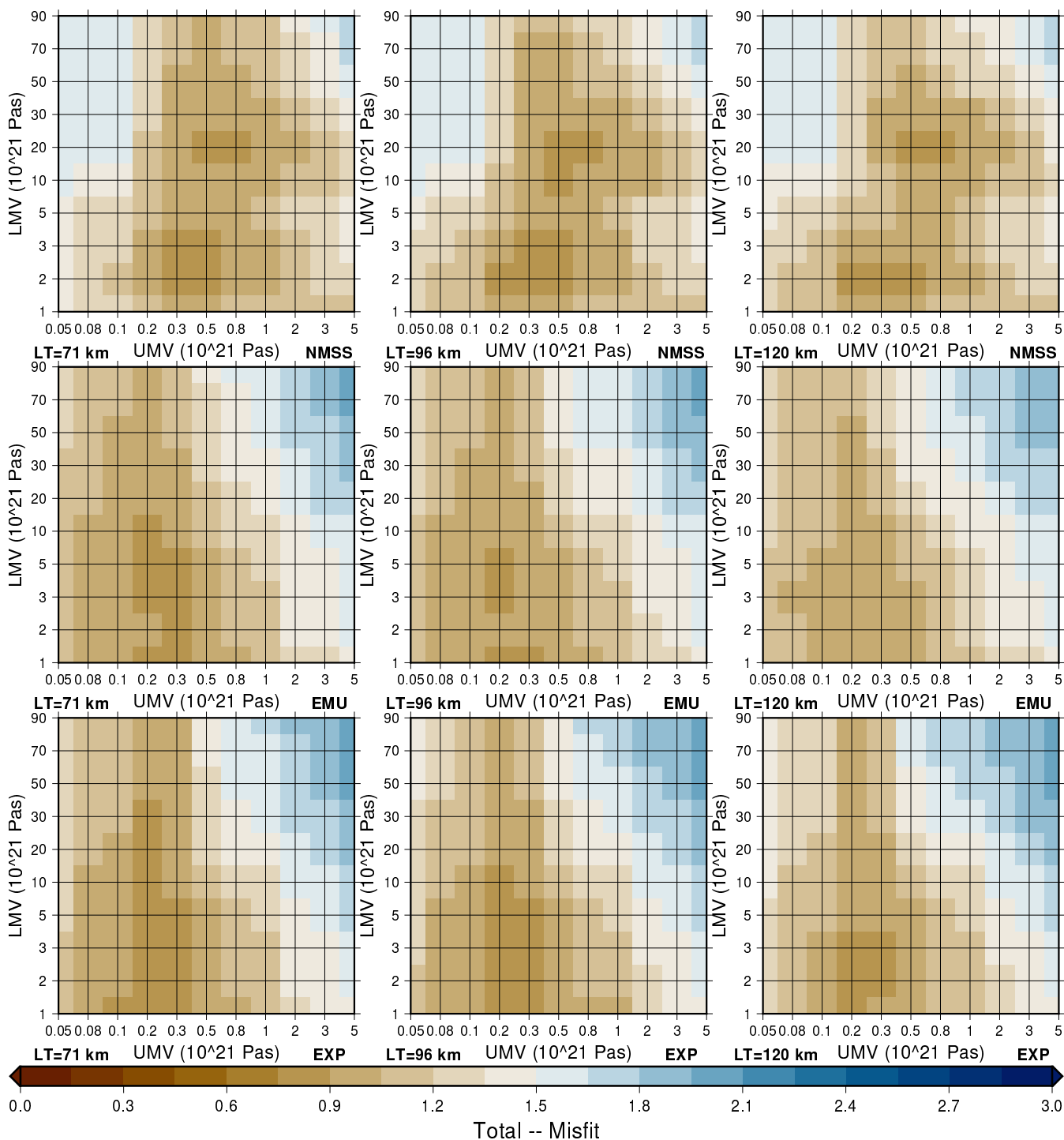
Figure 6. Plot shows proxy-data:model misfit for the North American RSL composite database for the NMSS model (top row), the emulator (EMU, middle row), and the explicit 3D-SS RSL output from Seakon added onto the NMSS RSL output (EXP, bottom row) from top-to-bottom respectively. Misfit varies as a function of global mean lithosphere thickness from left to right. Results are for the S40RTS+LR18 configuration.

database. Overall the proxy-data:model misfits calculated using the output of the emulator are more like the explicit results than the NMSS results alone. This result is obtained both visually and when considering the MSE values for the emulator:explicit and emulator:NMSS misfits. Since the emulator has more difficulty in reproducing the influence of lateral Earth structure in the intermediate field compared to near- and far-field locations (Fig. 5), it is interesting to compare the results for the USEC database (intermediate field) to the other two. For both the ice covered CAAC database and the relatively distant USGC database, the MSE of the emulator:explicit misfit results are one to two orders of magnitude smaller than the emulator:NMSS misfit. By comparison, for the USEC database which is largely near-to-intermediate field and also covers the fore-bulge region, the MSE of the emulator:explicit misfit results are the same order of magnitude as the emulator:NMSS misfit results.

The misfit data presented in Fig. 6 and Table 1 demonstrate that the emulator, as employed here, is successful both at reproducing the region in the LT/UMV/LMV parameter space which produces the lowest proxy-data:model misfits, and reproducing the relative values of proxy-data:model misfits throughout the parameter space. For both the CAAC and USGC subsets the use of the emulator results in a parameter vector with minimum misfit that is either the same or within 2 parameter value increments (with respect to the evaluated LT/UMV/LMV values) of the explicitly derived minimum misfit parameters. This accuracy is also obtained when considering the combined dataset. For all the databases examined, the parameter vector which produces the minimum misfit obtained by emulation is closer (in parameter space) to the explicit 3D-SS+NMSS case than the NMSS results. As such, using the emulator we are able to identify the region of LT/UMV/LMV parameter space that provides the optimum fits for a given lateral structure model (S40RTS+LR18). This smaller region of parameter space could then be explored using the explicit model to more accurately determine the optimal parameter vectors.

Previous work has typically used smaller regional-scale analyses to mitigate the influence of lateral Earth structure when using the assumption of spherical symmetry in the models of GIA & RSL (e.g., Love et al., 2016; Yousefi et al., 2018). The expectation is that as spatial scales grow larger, those Earth models which incorporate 3D structure will outperform SS Earth models. Examining the misfit results in Fig. 6 and Table 1, we do not find that the 3D Earth model considered here consistently outperforms SS Earth models on large spatial scales. For some cases, e.g. δ_{SLIP} for the US Gulf Coast, the 3D model results in a lower misfit by comparison to the SS model. However, that the 3D model results in lower proxy-data:model misfits on regional scales is expected given we are effectively adding, at least, two additional parameters to the model to find the minimum proxy-data:model misfit. Despite these findings, there are features in Fig. 6 which can be used to guide future investigations, e.g., the distribution and number of minima throughout the parameter space is different between the 3D and SS Earth models. The region of minimum misfit for the 3D Earth model is a fairly broad but defines a single minimum in the explored parameter space, rather than two distinct but relatively localized minima determined using the SS Earth models. There is a shift in the preferred UMV: for example, the UMV for the minimum misfit Earth model for the USEC δ_{slip} is 3×10^{21} Pa $\cdot$ s for the SS Earth model compared to 0.3×10^{21} Pa $\cdot$ s) for the 3D Earth model. This shows that radial viscosity structure inferred using a SS model can be significantly biased (e.g., Kuchar et al., 2019).

Overall, the SS Earth models still result in the lowest proxy-data:model misfits for the combined NA dataset. This suggests that our inputs to the 3D GIA model are incorrect. Given that we have investigated (for this study) only a single realization of lateral variability (to impose on a background SS Earth model) and a single ice sheet reconstruction, it is not possible to

determine which dominates (if any) in producing the higher than expected misfit results. Since ice sheet reconstructions (like ICE-6G) are developed assuming a SS GIA model, it not surprising that the SS Earth models outperform the 3D Earth models in ice covered areas such as the CAAC. This is also the reason why the optimum LT/UMV/LMV parameter set inferred here is a good approximation to the radial viscosity model assumed when constructing ICE-6G (i.e., VM5a).

Previous investigations (e.g., Gomez et al., 2018; van Calcar et al., 2023) demonstrate that coupling 3D Earth models to a dynamical ice sheet model applied to Antarctica results in considerable local ice thickness changes while not significantly impacting ice sheet volume when compared to results for a SS Earth model. Therefore, an important aim of future work will be to develop ice sheet models that are consistent with inferred 3D Earth structure. These more consistent 3D Earth-ice model pairings would hopefully result in improved fits to GIA-related data sets in near-field regions (compared to the SS Earth-ice model fits). In this regard, one potentially important extension of this work is to consider developing an ANN that can emulate results with different ice sheet histories. If successful, such an emulator could be used in coupled GIA-ice sheet models to include the effect of lateral variations in Earth structure. This would result in computation times that are equivalent to those for coupled SS GIA-ice sheet models (i.e., ≈ 10000 times more efficient vs. the reduced resolution configuration used in this study).

		δ_{SLIP}	δ_{ML}	δ_{TL}	δ_{Total}
CAAC					
NMSS	Minimum Misfit	0.075	0.021	0.108	0.383
	LT/UMV/LMV	96/0.30/2	46/0.80/5	120/0.80/90	71/0.50/2
EMU	Minimum Misfit	0.184	0.334	0.564	0.944
	LT/UMV/LMV	71/0.20/1	71/0.20/2	96/0.30/90	71/0.20/1
EXP	Minimum Misfit	0.188	0.286	0.566	0.885
	LT/UMV/LMV	71/0.20/2	71/0.30/2	120/0.80/90	71/0.20/1
US East Coast					
NMSS	Minimum Misfit	0.07	0	0	0.154
	LT/UMV/LMV	71/3.00/50			71/3.00/90
EMU	Minimum Misfit	0.064	0	0	0.125
	LT/UMV/LMV	71/0.50/50			120/0.50/30
EXP	Minimum Misfit	0.068	0	0	0.130
	LT/UMV/LMV	71/0.30/3			120/0.80/50
US Gulf Coast					
NMSS	Minimum Misfit	0.164	0.188	1.688	1.613
	LT/UMV/LMV	71/1.00/20	120/1.00/90	120/0.08/90	71/1.00/20
EMU	Minimum Misfit	0.149	0.179	1.959	1.619
	LT/UMV/LMV	96/0.05/3	120/0.80/90	120/0.08/90	96/0.05/3
EXP	Minimum Misfit	0.156	0.164	1.830	1.631
	LT/UMV/LMV	120/0.05/3	120/0.80/90	120/0.08/90	71/0.80/5
Combined NA					
NMSS	Minimum Misfit	0.091	0.288	0.977	0.823
	LT/UMV/LMV	96/0.30/2	46/0.50/2	71/0.10/90	96/0.30/2
EMU	Minimum Misfit	0.111	0.302	1.003	0.836
	LT/UMV/LMV	71/0.20/5	71/0.30/3	71/0.10/90	71/0.20/1
EXP	Minimum Misfit	0.103	0.273	0.969	0.823
	LT/UMV/LMV	71/0.20/2	71/0.30/3	71/0.10/90	71/0.20/2

Table 1. Misfits for the Canadian Arctic-Atlantic Coast (Vacchi et al., 2018), US East Coast (Engelhart and Horton, 2012), and US Gulf Coast (Hijma et al., 2015; Love et al., 2016) databases broken down into the contributing misfits for sea-level index points, marine & terrestrial limiting, and combined total as per Sect. 2.4. The lowest misfit for each of the data-types (i.e. SLIP, ML, TL, and total) and corresponding combination of SS lithospheric thickness(km), upper mantle viscosity($\times 10^{21}$ Pa·s), and lower mantle viscosity($\times 10^{21}$ Pa·s) are given for each region. Values are given for the NMSS model data, the emulator (ANN derived 3D-SS + NMSS), and explicit (Seakon 3D-SS + NMSS) data. Note that LT/UMV/LMV values for misfits of zero in the limiting data columns for the USEC are not unique and thus left blank.

4   Conclusions

This study provides an initial "proof of concept" assessment of using ANNs to emulate the influence of lateral Earth structure on GIA model output. We used the Tensorflow software library to produce ANNs, implement an emulator, and test the effectiveness of the emulator using model output of past (deglacial) sea-level change and present-day vertical land motion from a leading 3D (Earth) GIA model and a commonly used SS (Earth) GIA model. Our goal is to test whether the emulator can accurately predict the difference in these outputs (i.e., RSL and uplift rates) for the 3D case relative to the SS case. We pursued this application for two realisations of (global) lateral Earth structure (S40RTS, S40RTS+LR18, Ritsema et al., 2010; Afonso et al., 2019) and a commonly used ice history model (ICE6G, Peltier et al., 2015). Our results indicate that the emulator:model misfits, while not negligible, are of a scale such that useful predictions of deglacial RSL changes can be made. Evaluation of the emulator performance for deglacial RSL indicates that it is able to provide useful estimates of this field throughout the LT/UMV/LMV parameter space when trained on only $\approx 15\%$ (≈ 50) of the parameter vectors considered (330 in total). In contrast, results for present-day vertical land motion are poorer, with emulator errors of similar order to the 3D minus SS model output. Better results for emulating vertical land motion were obtained for model time steps when ice was still present, suggesting that the performance of the emulator (for present-day rates) could be improved by modifying inputs provided to the ANNs with respect to ice history. An important extension of this work is to consider different ice sheet models to determine if useful results can also be achieved for variations in this important GIA model parameter.

Given the relatively accurate results obtained for RSL, we applied the emulator in a proxy-data:model comparison exercise using RSL data distributed along North American coasts, from the Canadian Arctic to the US Gulf coast. The goals of this data:model comparison are two-fold: to determine if the emulator can produce accurate misfit values through the entire LT/UMV/LMV parameter space considered, and evaluate if the 3D Earth models can produced improved fits compared to the SS Earth models (for the chosen ice sheet and lateral Earth structure models). We find that the emulator is able to successfully reproduce the data:model misfit values such that the region of minimum misfit either overlaps the 3D GIA model results, or is within two increments in the parameter space. The emulator can, therefore, be used to more efficiently explore this aspect of the 3D Earth model parameter space. While the 3D Earth models can outperform the SS Earth models for some regional subsets of the RSL data set, the SS Earth models still produce better fits overall. Furthermore, the parameter values that give best fits for 3D and SS models are quite different, supporting previous work that show inferences of radial viscosity structure can be significantly biased when assuming SS structure. Thus, future work to further explore the parameter space of 3D Earth models and ice sheet histories is required.

Code and data availability. Software for training the artificial neural networks, model network weights, and the various utilities which comprise the emulator/surrogate model are available in the supplemental materials via Zenodo (Love et al., 2023a) and are licenced under the GNU Public Licence (GPL) v3. Example datasets, to use as templates and testing, are also included in the supplemental materials. Training data for the filtered datasets are available via Zenodo (Love et al., 2023b) and are licenced under the Creative Commons Attribution 4.0 licence. Unfiltered training data is available only upon request due to the large file-sizes involved. Additional model output beyond the

scope of the above availability statement may be available upon request. Source code for the GIA models used in this study are available

400 from their corresponding developers.

Competing interests. The authors declare that no competing interests are present.

5 Author Contributions

RL, GAM, PA, and LT contributed to the design and analysis of the ANNs. RL, GAM, and SP contributed to analysis and discussion. RL conducted all simulations and data processing with assistance from KL. RL and GAM prepared the manuscript

405 with contributions from all authors.

6 Acknowledgements

The authors would also like to thank those at the GNU and Fedora projects, Kernel.org, Tensorflow and in particular those responsible for GNU Parallel (Tange, 2011) whose software greatly sped up and streamlined the analysis in this work. This research was enabled in part by support provided by SciNet (www.scinethpc.ca) and the Digital Research Alliance of Canada

410 (formerly Compute Canada, https://alliancecan.ca) through the Rapid Access Service. RL, PA, SP, and GAM acknowledge funding support from the Natural Sciences and Engineering Research Council of Canada. LT acknowledges funding support from the PALMOD project.

References

Abadi, M., Agarwal, A., Barham, P., et al.: TensorFlow: Large-Scale Machine Learning on Heterogeneous Systems, https://www.tensorflow.org/, 2015.

Afonso, J. C., Salajegheh, F., Szwillus, W., Ebbing, J., and Gaina, C.: A global reference model of the lithosphere and upper mantle from joint inversion and analysis of multiple data sets, Geophysical Journal International, 217, 1602–1628, https://doi.org/10.1093/gji/ggz094, 2019.

Austermann, J., Mitrovica, J. X., Latychev, K., and Milne, G. A.: Barbados-based estimate of ice volume at Last Glacial Maximum affected by subducted plate, Nature Geoscience, 6, 553–557, https://doi.org/10.1038/ngeo1859, 2013.

Bagge, M., Klemann, V., Steinberger, B., Latinović, M., and Thomas, M.: Glacial-Isostatic Adjustment Models Using Geodynamically Constrained 3D Earth Structures, Geochemistry, Geophysics, Geosystems, 22, https://doi.org/10.1029/2021gc009853, 2021.

Baril, A., Garrett, E., Milne, G., Gehrels, W., and Kelley, J.: Postglacial relative sea-level changes in the Gulf of Maine, USA: Database compilation, assessment and modelling, Quaternary Science Reviews, 306, 108 027, https://doi.org/10.1016/j.quascirev.2023.108027, 2023.

Caron, L., Métivier, L., Greff-Lefftz, M., Fleitout, L., and Rouby, H.: Inverting Glacial Isostatic Adjustment signal using Bayesian framework and two linearly relaxing rheologies, Geophysical Journal International, 209, 1126–1147, https://doi.org/10.1093/gji/ggx083, 2017.

Chollet, F.: Deep learning with Python, Simon and Schuster, 2021.

Crawford, O., Al-Attar, D., Tromp, J., Mitrovica, J. X., Austermann, J., and Lau, H. C. P.: Quantifying the sensitivity of post-glacial sea level change to laterally varying viscosity, Geophysical Journal International, 214, 1324–1363, https://doi.org/10.1093/gji/ggy184, 2018.

Engelhart, S. E. and Horton, B. P.: Holocene sea level database for the Atlantic coast of the United States, Quaternary Science Reviews, 54, 12–25, https://doi.org/10.1016/j.quascirev.2011.09.013, 2012.

Farrell, W. E. and Clark, J. A.: On Postglacial Sea Level, Geophysical Journal of the Royal Astronomical Society, 46, 647–667, https://doi.org/10.1111/j.1365-246x.1976.tb01252.x, 1976.

Gomez, N., Latychev, K., and Pollard, D.: A Coupled Ice Sheet–Sea Level Model Incorporating 3D Earth Structure: Variations in Antarctica during the Last Deglacial Retreat, Journal of Climate, 31, 4041–4054, https://doi.org/10.1175/jcli-d-17-0352.1, 2018.

Hijma, M. P., Engelhart, S. E., Törnqvist, T. E., Horton, B. P., Hu, P., and Hill, D. F.: A protocol for a geological sea-level database, Handbook of Sea-Level Research, p. 536–553, https://doi.org/10.1002/9781118452547.ch34, 2015.

Jospin, L. V., Laga, H., Boussaid, F., Buntine, W., and Bennamoun, M.: Hands-On Bayesian Neural Networks—A Tutorial for Deep Learning Users, IEEE Computational Intelligence Magazine, 17, 29–48, https://doi.org/10.1109/mci.2022.3155327, 2022.

Karato, S.-i.: Deformation of earth materials, An introduction to the rheology of Solid Earth, 463, 2008.

Kendall, R. A., Mitrovica, J. X., and Milne, G. A.: On post-glacial sea level - II. Numerical formulation and comparative results on spherically symmetric models, Geophysical Journal International, 161, 679–706, https://doi.org/10.1111/j.1365-246x.2005.02553.x, 2005.

Klemann, V., Ivins, E. R., Martinec, Z., and Wolf, D.: Models of active glacial isostasy roofing warm subduction: Case of the South Patagonian Ice Field, Journal of Geophysical Research, 112, https://doi.org/10.1029/2006jb004818, 2007.

Kuchar, J., Milne, G., and Latychev, K.: The importance of lateral Earth structure for North American glacial isostatic adjustment, Earth and Planetary Science Letters, 512, 236–245, https://doi.org/10.1016/j.epsl.2019.01.046, 2019.

Lambeck, K., Rouby, H., Purcell, A., Sun, Y., and Sambridge, M.: Sea level and global ice volumes from the Last Glacial Maximum to the Holocene, Proceedings of the National Academy of Sciences, 111, 15 296–15 303, https://doi.org/10.1073/pnas.1411762111, 2014.

Latychev, K., Mitrovica, J. X., Tromp, J., Tamisiea, M. E., Komatitsch, D., and Christara, C. C.: Glacial isostatic adjustment on 3-D Earth
450   models: a finite-volume formulation, Geophysical Journal International, 161, 421–444, https://doi.org/10.1111/j.1365-246x.2005.02536.x,
       2005.

Li, T., Khan, N. S., Baranskaya, A. V., Shaw, T. A., Peltier, W. R., Stuhne, G. R., Wu, P., and Horton, B. P.: Influence of
       3D Earth Structure on Glacial Isostatic Adjustment in the Russian Arctic, Journal of Geophysical Research: Solid Earth, 127,
       https://doi.org/10.1029/2021jb023631, 2022.

455   Love, R., Milne, G. A., Tarasov, L., Engelhart, S. E., Hijma, M. P., Latychev, K., Horton, B. P., and Törnqvist, T. E.: The contribution of
       glacial isostatic adjustment to projections of sea-level change along the Atlantic and Gulf coasts of North America, Earth's Future, 4,
       440–464, https://doi.org/10.1002/2016ef000363, 2016.

Love, R., Milne, G. A., Ajourlou, P., Parang, S., Tarasov, L., and Latychev, K.: Supplemental Materials for A Fast Surrogate Model for
       3D-Earth Glacial Isostatic Adjustment using Tensorflow (v2.8.10) Artificial Neural Networks, https://doi.org/10.5281/zenodo.10045462,
460   2023a.

Love, R., Milne, G. A., Ajourlou, P., Parang, S., Tarasov, L., and Latychev, K.: Input Data for A Fast Surrogate Model for 3D-Earth Glacial
       Isostatic Adjustment using Tensorflow (v2.8.10) Artificial Neural Networks, https://doi.org/10.5281/zenodo.10042047, 2023b.

Milne, G. A.: Glacial isostatic adjustment, Handbook of Sea-Level Research, p. 419–437, https://doi.org/10.1002/9781118452547.ch28,
       2015.

465   Mitrovica, J. X. and Milne, G. A.: On post-glacial sea level: I. General theory, Geophysical Journal International, 154, 253–267,
       https://doi.org/10.1046/j.1365-246x.2003.01942.x, 2003.

Mitrovica, J. X. and Peltier, W. R.: A comparison of methods for the inversion of viscoelastic relaxation spectra, Geophysical Journal
       International, 108, 410–414, https://doi.org/10.1111/j.1365-246x.1992.tb04623.x, 1992.

Pan, L., Milne, G. A., Latychev, K., Goldberg, S. L., Austermann, J., Hoggard, M. J., and Mitrovica, J. X.: The influence of lateral
470   Earth structure on inferences of global ice volume during the Last Glacial Maximum, Quaternary Science Reviews, 290, 107 644,
       https://doi.org/10.1016/j.quascirev.2022.107644, 2022.

Paulson, A., Zhong, S., and Wahr, J.: Modelling post-glacial rebound with lateral viscosity variations, Geophysical Journal International,
       163, 357–371, https://doi.org/10.1111/j.1365-246x.2005.02645.x, 2005.

Paulson, A., Zhong, S., and Wahr, J.: Inference of mantle viscosity from GRACE and relative sea level data, Geophysical Journal Interna-
475   tional, 171, 497–508, https://doi.org/10.1111/j.1365-246x.2007.03556.x, 2007.

Peltier, W. R.: The impulse response of a Maxwell Earth, Reviews of Geophysics, 12, 649, https://doi.org/10.1029/rg012i004p00649, 1974.

Peltier, W. R.: Glacial-Isostatic Adjustment-II. The Inverse Problem, Geophysical Journal of the Royal Astronomical Society, 46, 669–705,
       https://doi.org/10.1111/j.1365-246x.1976.tb01253.x, 1976.

Peltier, W. R., Argus, D. F., and Drummond, R.: Space geodesy constrains ice age terminal deglaciation: The global ICE6GC (VM5a) model,
480   Journal of Geophysical Research: Solid Earth, 120, 450–487, https://doi.org/10.1002/2014jb011176, 2015.

Powell, E. M., Pan, L., Hoggard, M. J., Latychev, K., Gomez, N., Austermann, J., and Mitrovica, J. X.: The impact of 3-D Earth
       structure on far-field sea level following interglacial West Antarctic Ice Sheet collapse, Quaternary Science Reviews, 273, 107 256,
       https://doi.org/10.1016/j.quascirev.2021.107256, 2021.

Ritsema, J., Deuss, A., van Heijst, H. J., and Woodhouse, J. H.: S40RTS: a degree-40 shear-velocity model for the mantle from new
485   Rayleigh wave dispersion, teleseismic traveltime and normal-mode splitting function measurements, Geophysical Journal International,
       184, 1223–1236, https://doi.org/10.1111/j.1365-246x.2010.04884.x, 2010.

Roy, K. and Peltier, W.: Space-geodetic and water level gauge constraints on continental uplift and tilting over North America: regional convergence of the ICE-6G_C (VM5a/VM6) models, Geophysical Journal International, 210, 1115–1142, https://doi.org/10.1093/gji/ggx156, 2017.

490 Sellevold, R. and Vizcaino, M.: First Application of Artificial Neural Networks to Estimate 21st Century Greenland Ice Sheet Surface Melt, Geophysical Research Letters, 48, https://doi.org/10.1029/2021gl092449, 2021.

Shepherd, A., Ivins, E. R., A, G., Barletta, V. R., Bentley, M. J., Bettadpur, S., Briggs, K. H., Bromwich, D. H., Forsberg, R., Galin, N., Horwath, M., Jacobs, S., Joughin, I., King, M. A., Lenaerts, J. T. M., Li, J., Ligtenberg, S. R. M., Luckman, A., Luthcke, S. B., McMillan, M., Meister, R., Milne, G., Mouginot, J., Muir, A., Nicolas, J. P., Paden, J., Payne, A. J., Pritchard, H., Rignot, E., Rott, H., Sørensen,

495 L. S., Scambos, T. A., Scheuchl, B., Schrama, E. J. O., Smith, B., Sundal, A. V., van Angelen, J. H., van de Berg, W. J., van den Broeke, M. R., Vaughan, D. G., Velicogna, I., Wahr, J., Whitehouse, P. L., Wingham, D. J., Yi, D., Young, D., and Zwally, H. J.: A Reconciled Estimate of Ice-Sheet Mass Balance, Science, 338, 1183–1189, https://doi.org/10.1126/science.1228102, 2012.

Spada, G.: Glacial Isostatic Adjustment and Contemporary Sea Level Rise: An Overview, pp. 155–187, Springer International Publishing, https://doi.org/10.1007/978-3-319-56490-6_8, 2017.

500 Steffen, H. and Kaufmann, G.: Glacial isostatic adjustment of Scandinavia and northwestern Europe and the radial viscosity structure of the Earth's mantle, Geophysical Journal International, 163, 801–812, https://doi.org/10.1111/j.1365-246x.2005.02740.x, 2005.

Steffen, H., Denker, H., and Müller, J.: Glacial isostatic adjustment in Fennoscandia from GRACE data and comparison with geodynamical models, Journal of Geodynamics, 46, 155–164, https://doi.org/10.1016/j.jog.2008.03.002, 2008.

Tange, O.: GNU Parallel - The Command-Line Power Tool, ;login: The USENIX Magazine, 36, 42–47, http://www.gnu.org/s/parallel, 2011.

505 Tarasov, L., Dyke, A. S., Neal, R. M., and Peltier, W.: A data-calibrated distribution of deglacial chronologies for the North American ice complex from glaciological modeling, Earth and Planetary Science Letters, 315–316, 30 – 40, https://doi.org/http://dx.doi.org/10.1016/j.epsl.2011.09.010, sea Level and Ice Sheet Evolution: A {PALSEA} Special Edition, 2012.

Vacchi, M., Engelhart, S. E., Nikitina, D., et al.: Postglacial relative sea-level histories along the eastern Canadian coastline, QSR, 201, 124–146, https://doi.org/10.1016/j.quascirev.2018.09.043, 2018.

510 van Calcar, C. J., van de Wal, R. S. W., Blank, B., de Boer, B., and van der Wal, W.: Simulation of a fully coupled 3D glacial isostatic adjustment – ice sheet model for the Antarctic ice sheet over a glacial cycle, Geoscientific Model Development, 16, 5473–5492, https://doi.org/10.5194/gmd-16-5473-2023, 2023.

van der Wal, W., Wu, P., Sideris, M. G., and Shum, C.: Use of GRACE determined secular gravity rates for glacial isostatic adjustment studies in North-America, Journal of Geodynamics, 46, 144–154, https://doi.org/10.1016/j.jog.2008.03.007, 2008.

515 van der Wal, W., Barnhoorn, A., Stocchi, P., Gradmann, S., Wu, P., Drury, M., and Vermeersen, B.: Glacial isostatic adjustment model with composite 3-D Earth rheology for Fennoscandia, Geophysical Journal International, 194, 61–77, https://doi.org/10.1093/gji/ggt099, 2013.

van der Wal, W., Whitehouse, P. L., and Schrama, E. J.: Effect of GIA models with 3D composite mantle viscosity on GRACE mass balance estimates for Antarctica, Earth and Planetary Science Letters, 414, 134–143, https://doi.org/10.1016/j.epsl.2015.01.001, 2015.

Wang, H., Wu, P., and van der Wal, W.: Using postglacial sea level, crustal velocities and gravity-rate-of-change to constrain the influence of

520 thermal effects on mantle lateral heterogeneities, Journal of Geodynamics, 46, 104–117, https://doi.org/10.1016/j.jog.2008.03.003, 2008.

Whitehouse, P., Latychev, K., Milne, G. A., Mitrovica, J. X., and Kendall, R.: Impact of 3-D Earth structure on Fennoscandian glacial isostatic adjustment: Implications for space-geodetic estimates of present-day crustal deformations, Geophysical Research Letters, 33, https://doi.org/10.1029/2006gl026568, 2006.

Whitehouse, P. L.: Glacial isostatic adjustment modelling: historical perspectives, recent advances, and future directions, Earth Surface
525 Dynamics, 6, 401–429, https://doi.org/10.5194/esurf-6-401-2018, 2018.

Williams, C., Lord, N., Lunt, D., Kennedy-Asser, A., Richards, D., Crucifix, M., Kontula, A., Thorne, M., Valdes, P., Foster, G., and Mc-
Clymont, E.: The relative role of orbital, CO_2 and ice sheet forcing on Pleistocene climate, https://doi.org/10.5194/egusphere-egu23-1048,
2023.

Wu, P.: Effects of lateral variations in lithospheric thickness and mantle viscosity on glacially induced surface motion in Laurentia, Earth and
530 Planetary Science Letters, 235, 549–563, https://doi.org/10.1016/j.epsl.2005.04.038, 2005.

Yousefi, M., Milne, G. A., Love, R., and Tarasov, L.: Glacial isostatic adjustment along the Pacific coast of central North America, Quaternary
Science Reviews, 193, 288–311, https://doi.org/10.1016/j.quascirev.2018.06.017, 2018.

Supplemental Materials: A Fast Surrogate Model for 3D-Earth Glacial Isostatic Adjustment using Tensorflow (v2.8.10) Artificial Neural Networks

Ryan Love[1], Glenn A. Milne[1], Parviz Ajourlou[1], Soran Parang[1], Lev Tarasov[2], and Konstantin Latychev[3]

[1]Department of Earth Sciences, University of Ottawa, Ottawa, Ontario, Canada
[2]Department of Physics and Physical Oceanography, Memorial University of Newfoundland, St. John's, Newfoundland, Canada
[3]SEAKON, Toronto, Canada

Correspondence: Ryan Love (rlove@mun.ca)

S1   Supplemental Figures
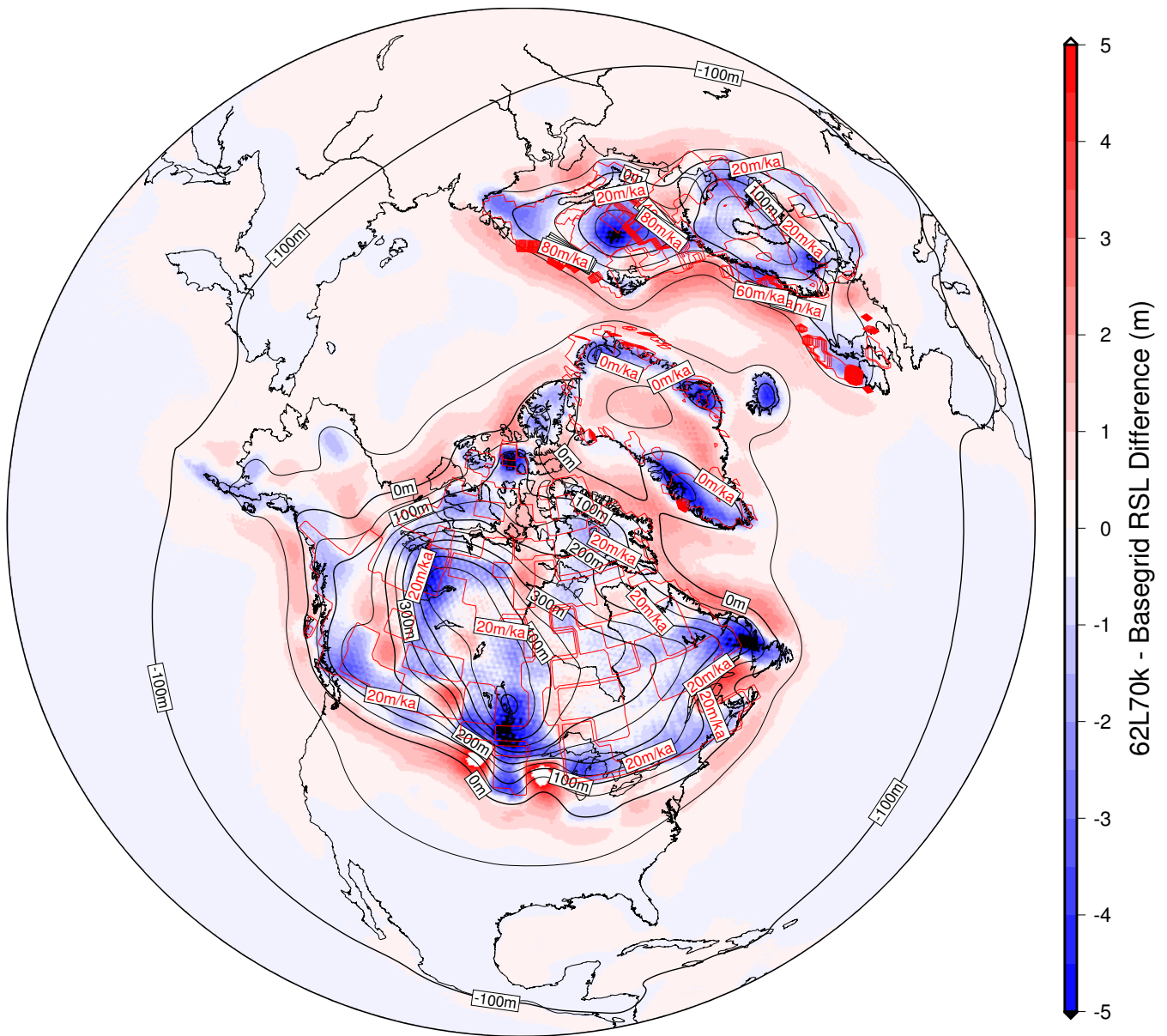
Figure S1. Difference in predicted RSL at LGM between a reduced resolution configuration (62L70k) and the more typical Seakon resolution (Basegrid). Black contours denote the RSL field from the Basegrid configuration at 50m intervals. The average rate of change in ice thickness between 21 ka and 25 ka, expressed in m/ka, are contoured in red at 10 m/ka intervals. These results are for the ICE5G (Peltier, 2004) ice loading history and background radial viscosity profile of a 120 km thick elastic lithosphere, 3×10^{21} Pa·s upper mantle viscosity, and 90×10^{21} Pa·s lower mantle viscosity. This SS profile was chosen as it performed well for the USEC database in previous investigations (Love et al., 2016). The Seakon model results shown here are comparisons between spherically symmetric configurations. Tests involving lateral variability structure give comparable results.

Figure S2. Locations of sea-level index points, terrestrial limiting, marine limiting data are shown as coloured symbols. The shape and colour reflect the groupings of each data-point. VS01 through VS35 are sites 1 through 35 from Vacchi et al. (2018). Connecticut through to S. South-Carolina are from Engelhart and Horton (2012). S.E. Florida to S. Texas are from Love et al. (2016).
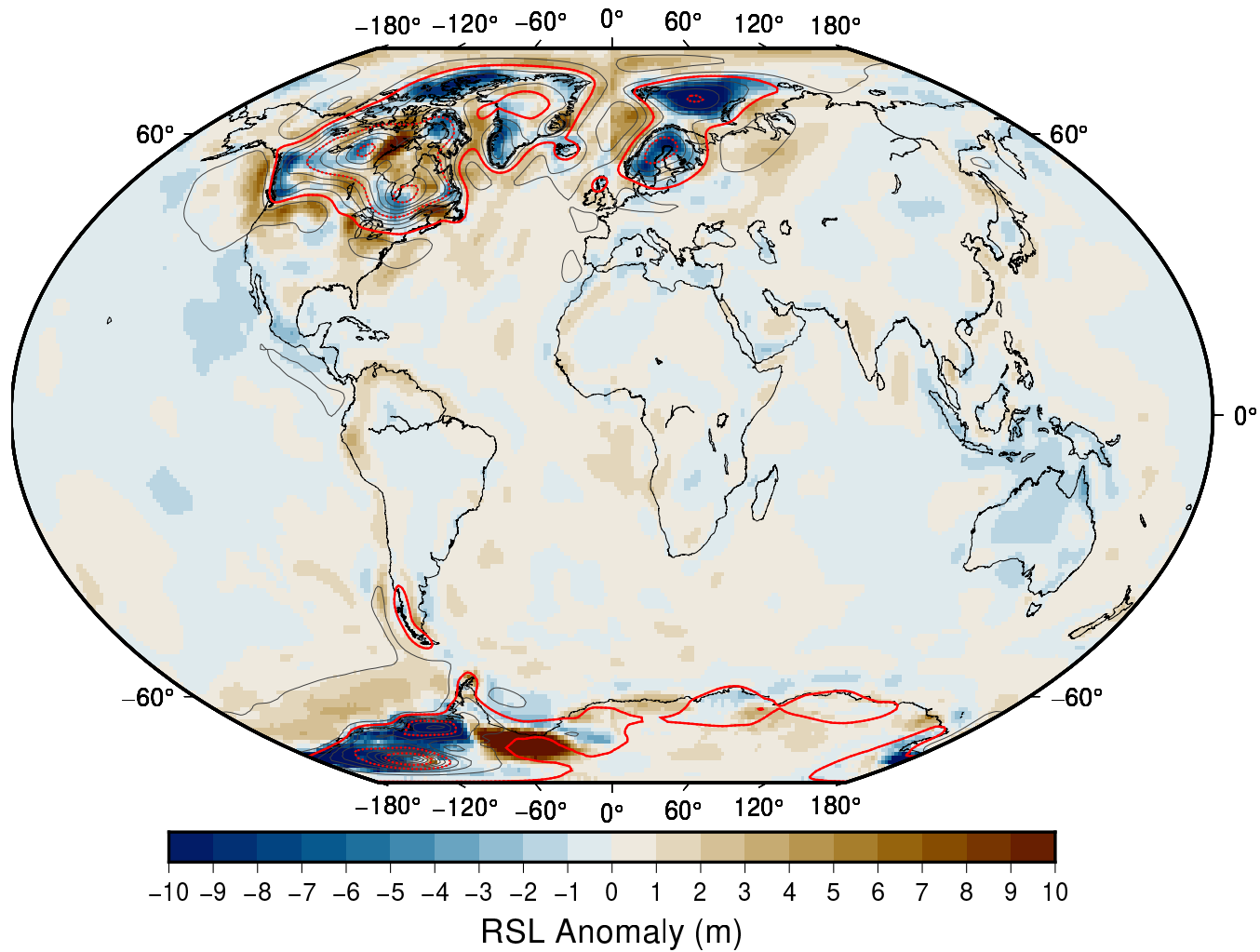
Figure S3. RSL anomaly, emulated RSL field minus explicit (3D-SS Seakon + NMSS) RSL field for the S40RTS+LR18 case, at 10 ka. Grey contours denote the RSL field (from Seakon) in 25 m increments, dotted red contours denote 100 m increments, and the solid red contour denotes the 0 m contour. The parameter vector plotted is that with the median MSE, calculated for all spatio-temporal data, for the N = 45 results.
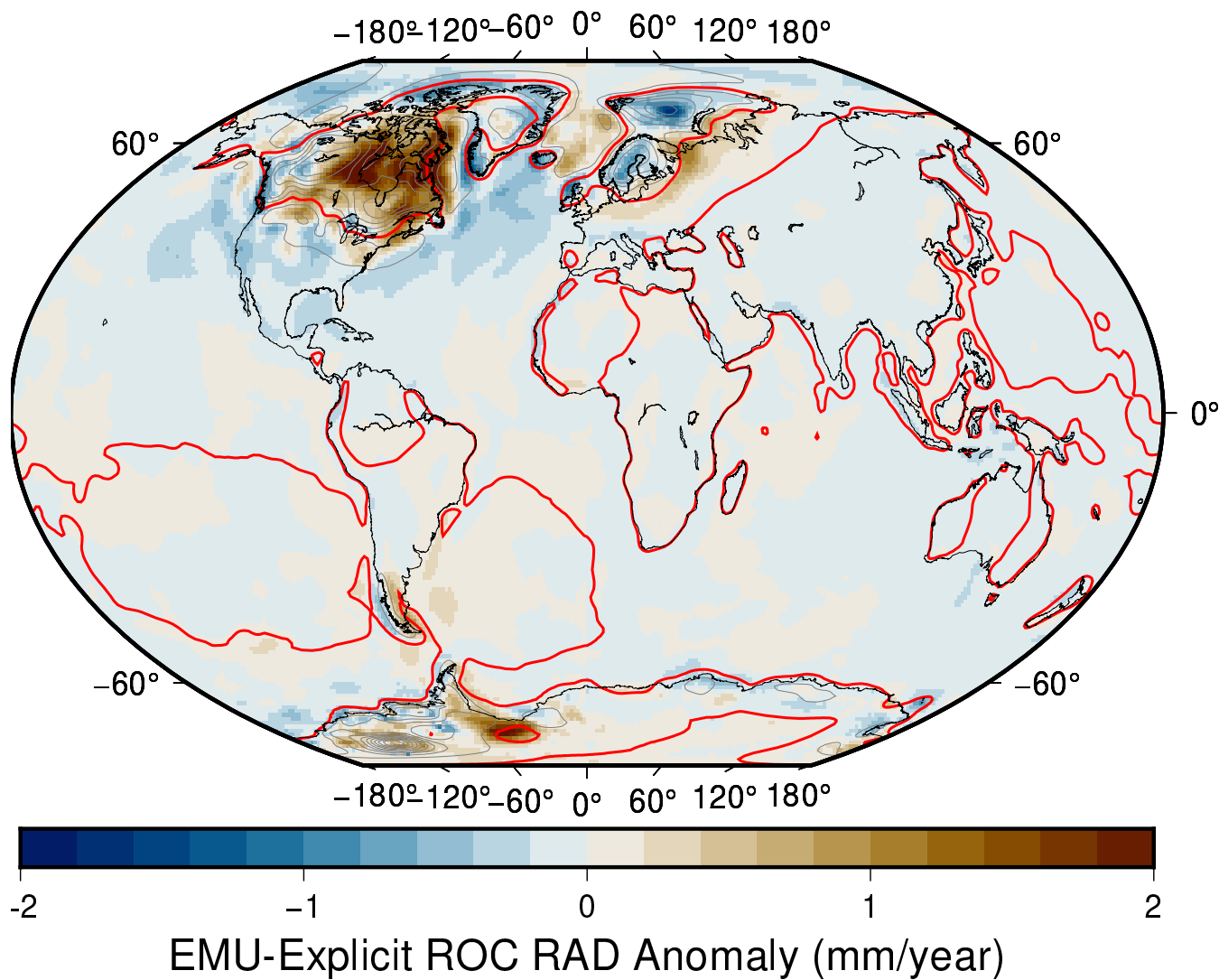
Figure S4. ROC RAD anomaly, emulated field minus 3D-SS field added to the NMSS output for the S40RTS+LR18 case, at present day. Contours denote the ROC RAD field (from from 3D-SS+NMSS) in 2 mm/yr increments, the red line denotes the 0 mm/yr contour. The parameter vector plotted is that with the median MSE, calculated for all spatio-temporal data, for the N = 45 ANN.
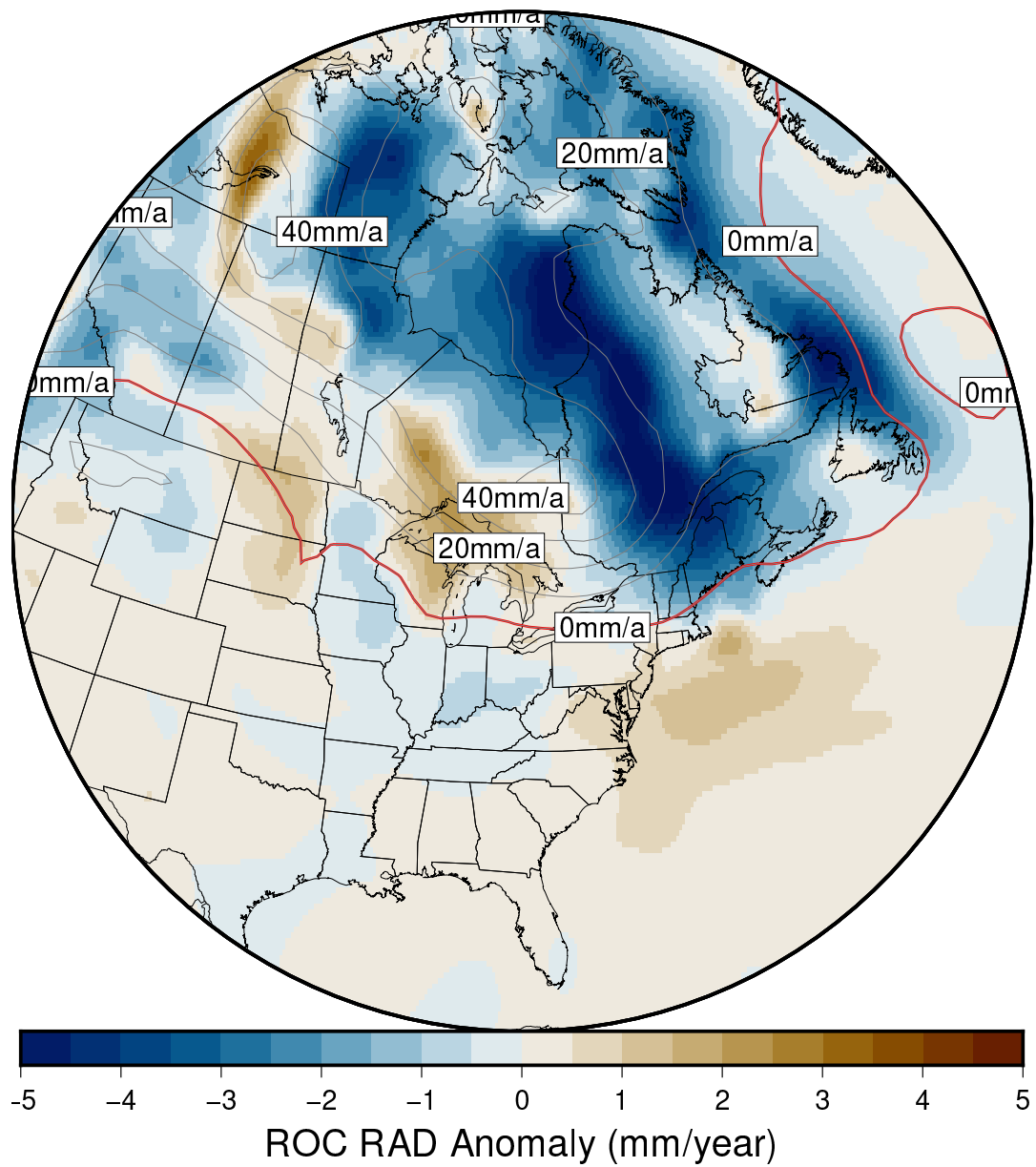
Figure S5. ROC RAD anomaly, emulated field minus 3D-SS field added to the NMSS output for the S40RTS+LR18 case, at 10ka. Contours denote the ROC RAD field (from from 3D-SS+NMSS) in 10 mm/yr increments, the red line denotes the 0 mm/yr contour. The parameter vector plotted is that with the median MSE, calculated for all spatio-temporal data, for the N = 45 ANN.
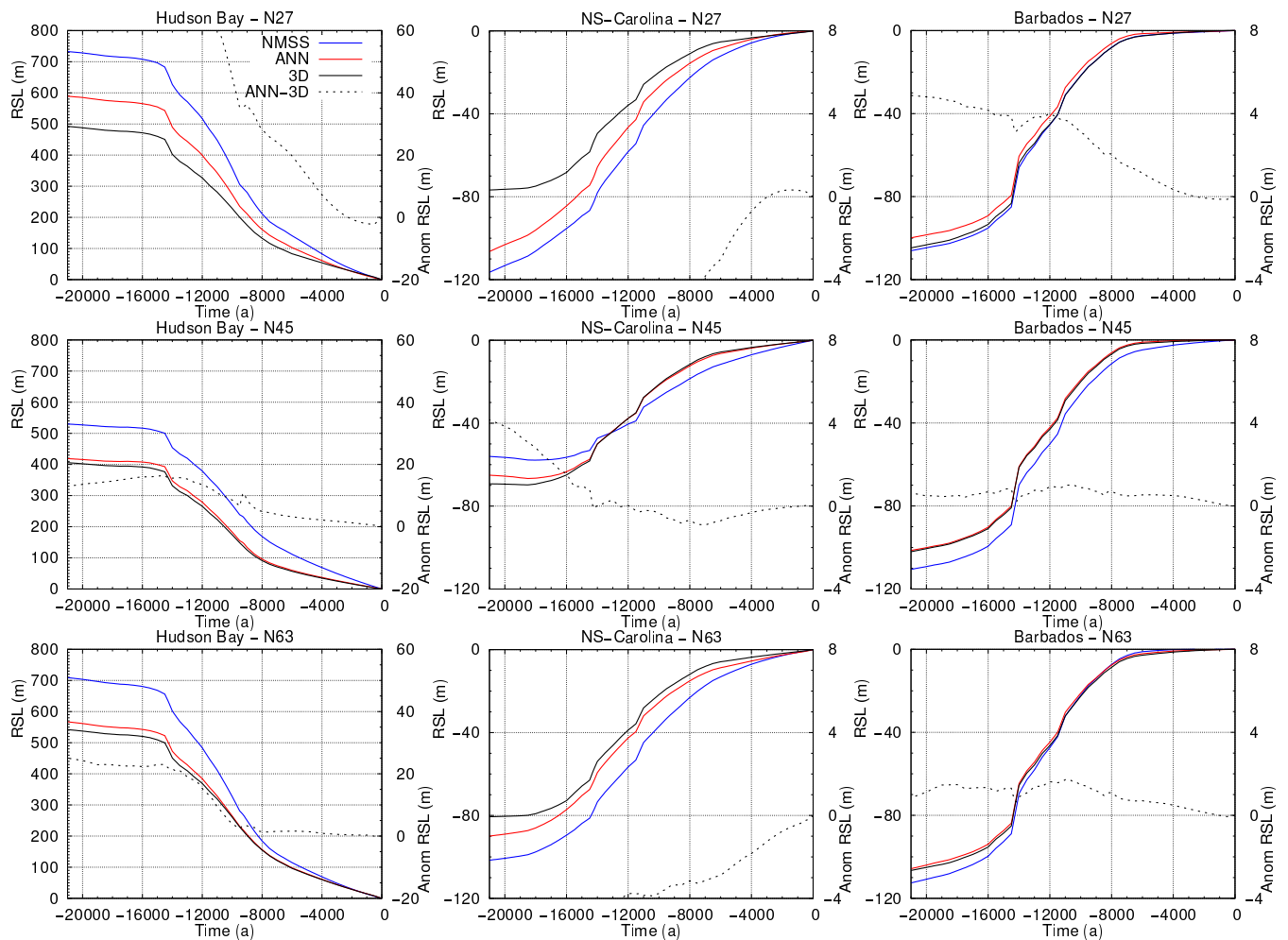
Figure S6. RSL timeseries for a near/ice-covered (Hudson Bay), intermediate (Northern S-Carolina), and far-field (Barbados) locations, for three of the trained ANNs which feature a reduced set of training ensemble members (number of parameter vectors included are denoted by N). Parameter vectors shown are drawn from the validation ensemble and are the median members (when considering the full spatio-temporal mean square error of the ANN). 3D Earth model configuration shown is the S40RTS with a SS lithosphere.
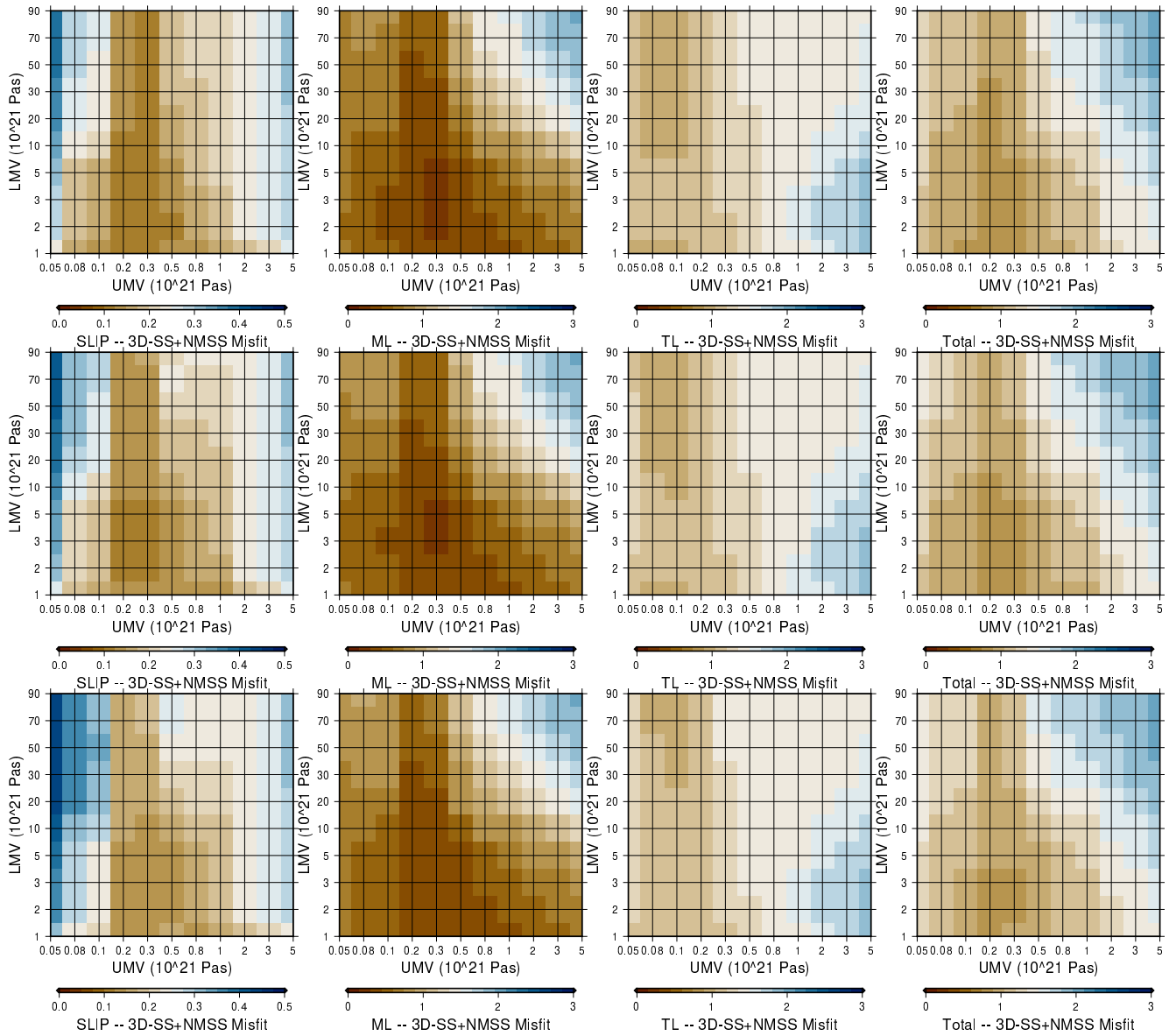
Figure S7. Misfit over parameter vectors for combined RSL database using explicit 3D model output (NMSS plus 3D-SS from Seakon) for S40RTS+LR18. Rows are different lithosphere thicknesses (71, 96, and 120km from top to bottom respectively).
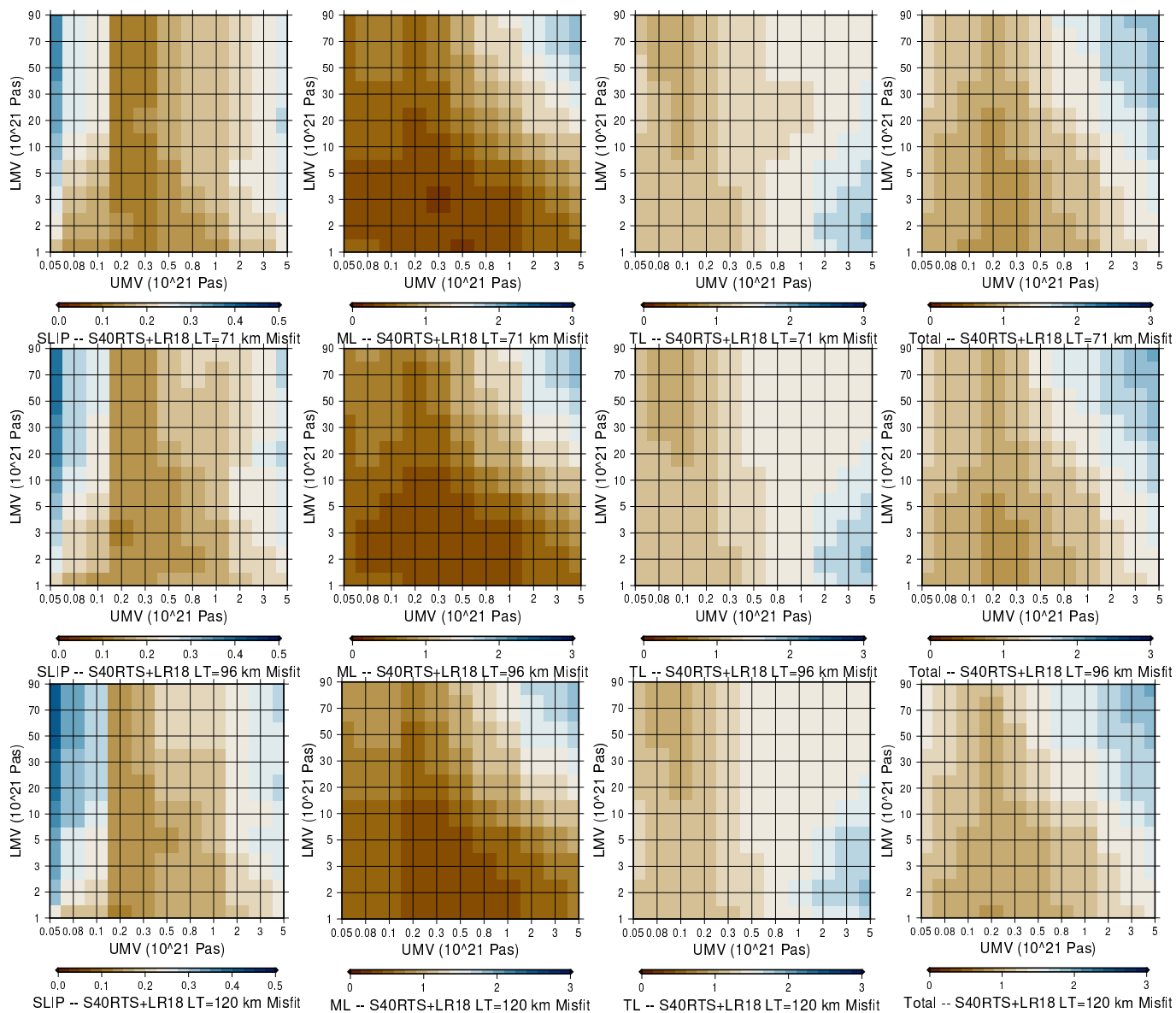
Figure S8. Plot shows misfit for the combined RSL database through parameter space (LT/UMV/LMV) for the NMSS model modified with the ANN to emulate S40RTS with the LR18 lithosphere model 3D Earth model. Columns from left to right show marine limiting, SLIP, terrestrial limiting, and total misfits respectively, while rows are 71, 96, and 120 km respectively. Misfit plotted is calculated as in equations 1 and 2.
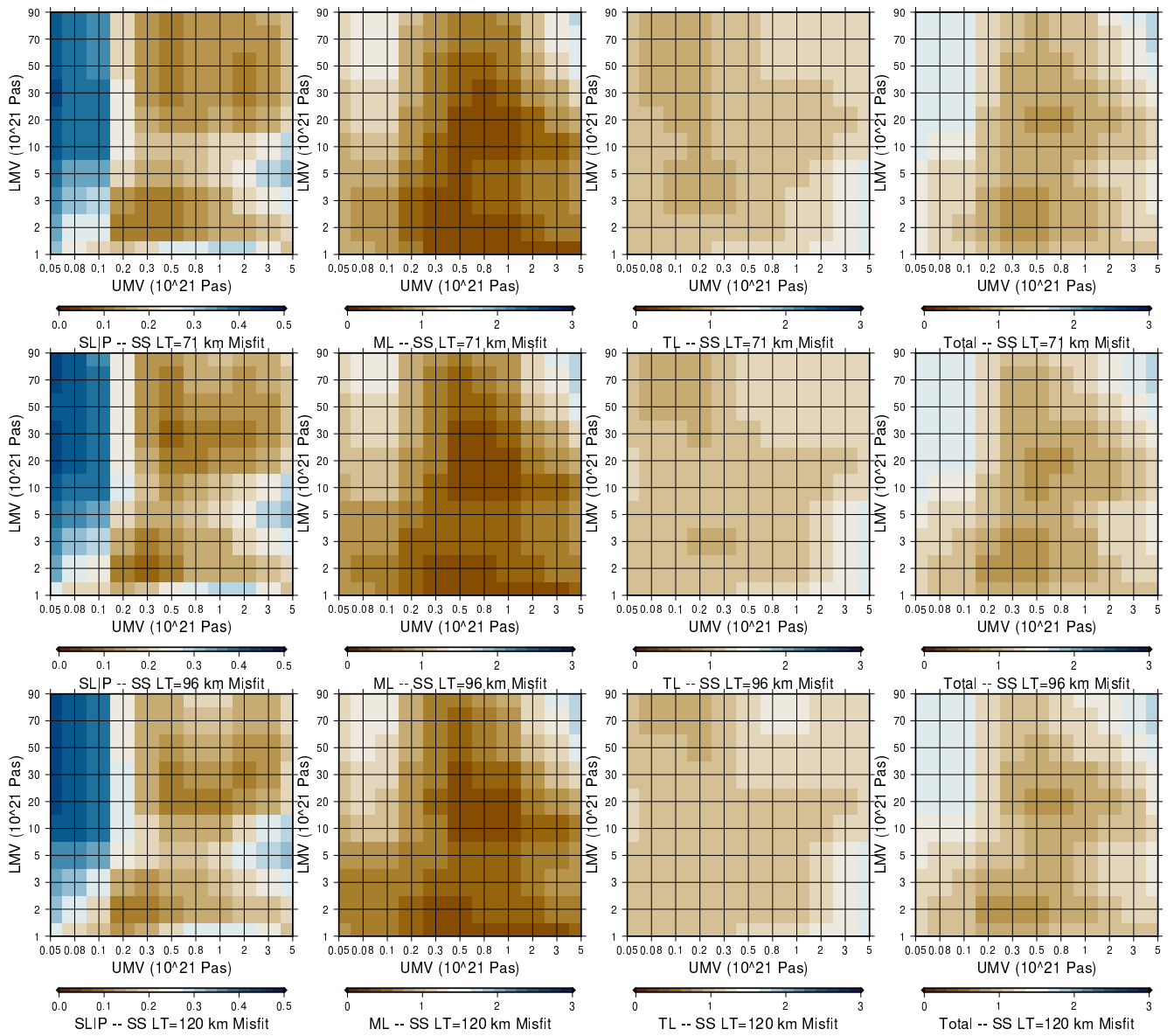
Figure S9. Plot shows misfit for the combined RSL database through parameter space (LT/UMV/LMV) for the NMSS model. Columns from left to right show marine limiting, SLIP, terrestrial limiting, and total misfits respectively, while rows are 71, 96, and 120 km respectively. Misfit plotted is calculated as in equations 1 and 2.
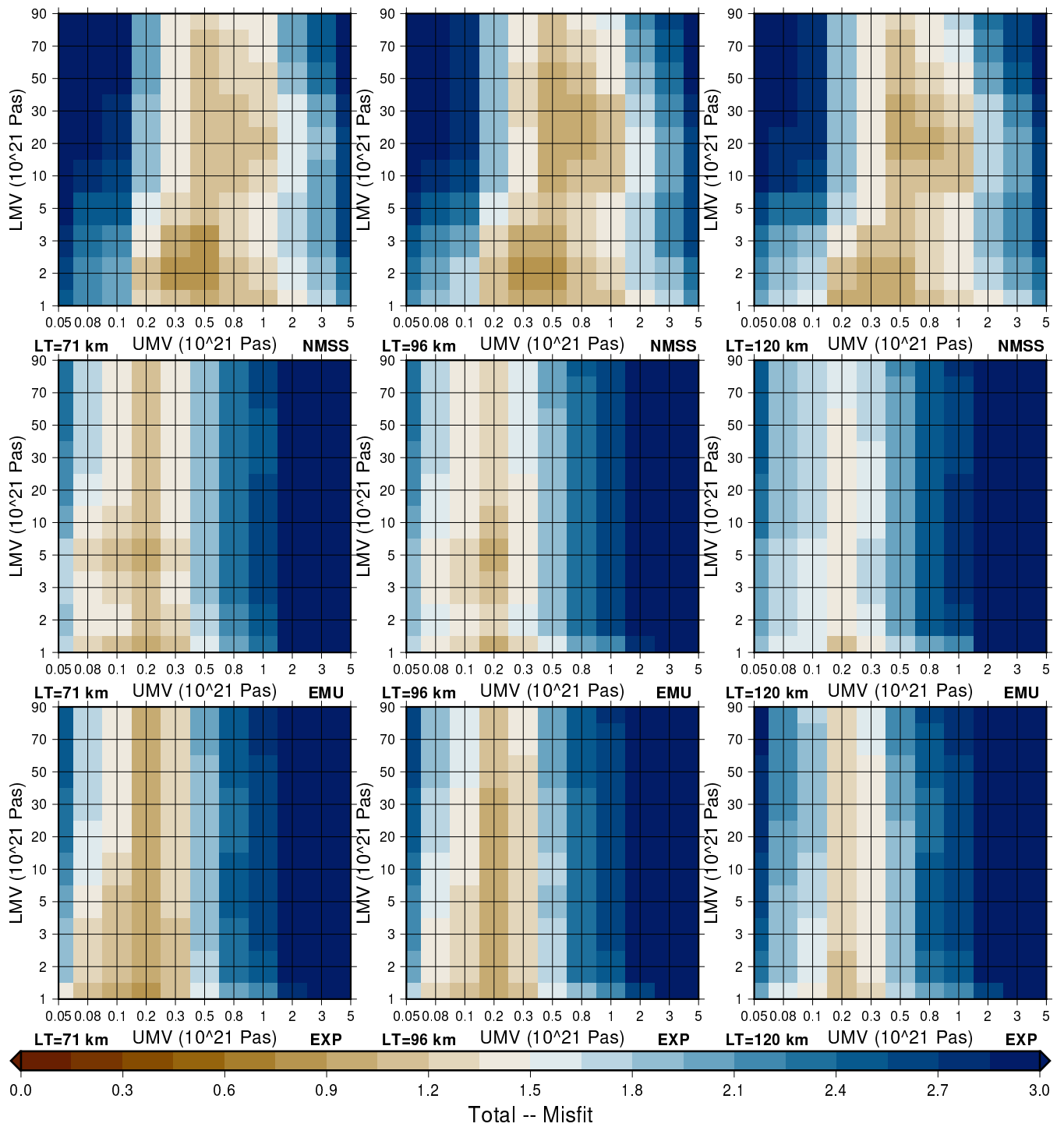
Figure S10. Model:data misfit across the CAAC RSL database through parameter space (LT/UMV/LMV). Top row is NMSS model output, middle row is emulated 3D model output (NMSS plus emulated 3D-SS from Seakon), bottom row is explicit (NMSS plus 3D-SS from Seakon) output. Misfit plotted is calculated as in equations 1 and 2 and total misfit has been plotted.
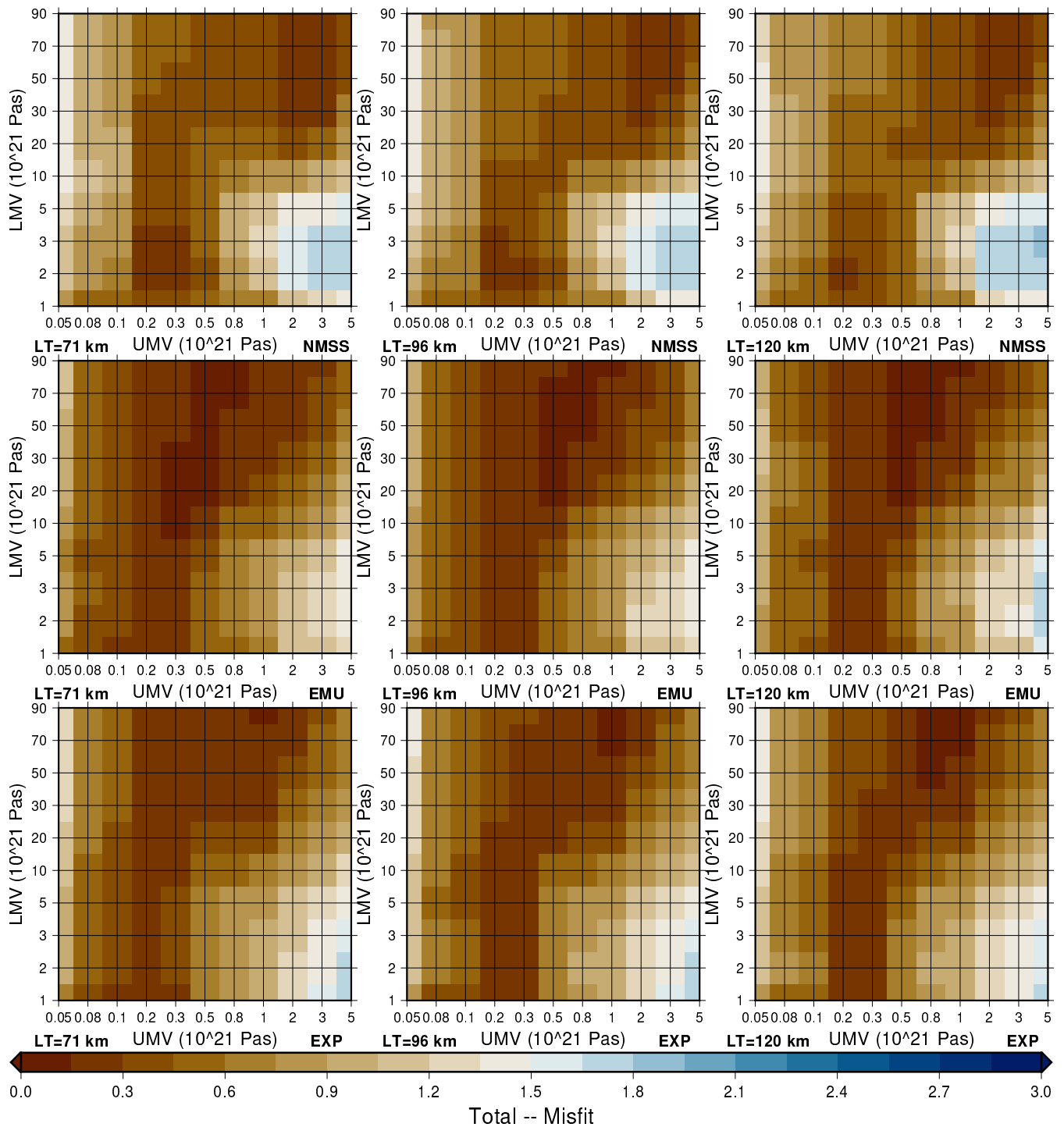
Figure S11. Model:data misfit across the USEC RSL database through parameter space (LT/UMV/LMV). Top row is NMSS model output, middle row is emulated 3D model output (NMSS plus emulated 3D-SS from Seakon), bottom row is explicit (NMSS plus 3D-SS from Seakon) output. Misfit plotted is calculated as in equations 1 and 2 and total misfit has been plotted.
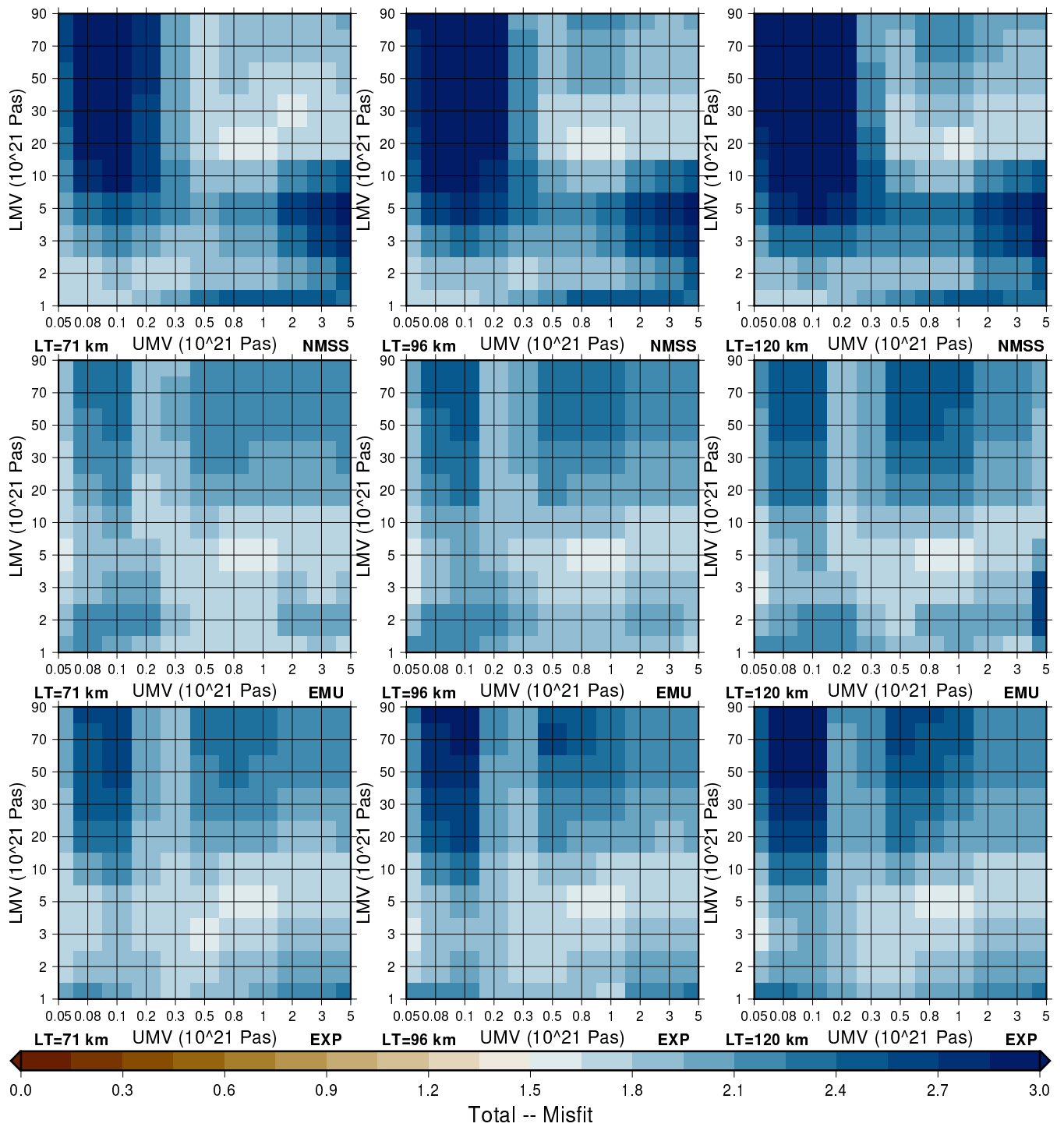
Figure S12. Model:data misfit across the USGC RSL database through parameter space (LT/UMV/LMV). Top row is NMSS model output, middle row is emulated 3D model output (NMSS plus emulated 3D-SS from Seakon), bottom row is explicit (NMSS plus 3D-SS from Seakon) output. Misfit plotted is calculated as in equations 1 and 2 and total misfit has been plotted.

References

Engelhart, S. E. and Horton, B. P.: Holocene sea level database for the Atlantic coast of the United States, Quaternary Science Reviews, 54, 12–25, https://doi.org/10.1016/j.quascirev.2011.09.013, 2012.

5 Love, R., Milne, G. A., Tarasov, L., Engelhart, S. E., Hijma, M. P., Latychev, K., Horton, B. P., and Törnqvist, T. E.: The contribution of glacial isostatic adjustment to projections of sea-level change along the Atlantic and Gulf coasts of North America, Earth's Future, 4, 440–464, https://doi.org/10.1002/2016ef000363, 2016.

Peltier, W.: GLOBAL GLACIAL ISOSTASY AND THE SURFACE OF THE ICE-AGE EARTH: The ICE-5G (VM2) Model and GRACE, Annual Review of Earth and Planetary Sciences, 32, 111–149, https://doi.org/10.1146/annurev.earth.32.082503.144359, 2004.

10 Vacchi, M., Engelhart, S. E., Nikitina, D., et al.: Postglacial relative sea-level histories along the eastern Canadian coastline, QSR, 201, 124–146, https://doi.org/10.1016/j.quascirev.2018.09.043, 2018.